NUMERICAL MODELING OF MICROSCALE MIXING USING LATTICE BOLTZMANN METHOD

ANINDYA KANTI DE

Dissertation submitted to the faculty of the Virginia Polytechnic Institute and State University in partial fulfillment of the requirements for the degree of

Doctor of Philosophy
In
Engineering Mechanics

Academic Committee

Prof. Ishwar K. Puri, Committee Chair

(The committee members are listed in alphabetical order)

Prof. Hassan Aref

Prof. Mark S. Cramer

Prof. Mayuresh J. Patil

Prof. Michael W. Hyer

April 28th, 2008
Blacksburg, VA

Keywords: Mixing, microscale, magnetic fluid, electroosmosis, lattice Boltzmann method.

NUMERICAL MODELING OF MICROSCALE MIXING USING LATTICE BOLTZMANN METHOD

ANINDYA KANTI DE

ABSTRACT

Recent advancements in microfabrication technology have led to the development of micro-total analytical systems (μ-TAS), more popularly known as *lab-on-a-chip* (*LOC*) devices. These devices have a relatively small size and are capable of performing sample and reagent handling steps together with analytical measurements. Rapid mixing is essential in such microfluidic systems for various applications e.g., biochemical analysis, sequencing or synthesis of nucleic acids, and for reproducible biological processes that involve cell activation, enzyme reactions, and protein folding.

In this work a numerical model is developed using a lattice Boltzmann method (LBM) to study microscale mixing. The study involves two mixing methods, namely, electroosmotic mixing and magnetic assisted mixing. A single component LBM model is developed to study electroosmotic flow in a square cavity. Mixing is studied by introducing two types of tracer particles in the steady electroosmotic flow and characterized by various mixing parameters. The results show that rapid mixing can be achieved by using a steady electric field and a homogeneous zeta potential.

A multicomponent LBM method is also developed to study magnetic assisted mixing in a channel configuration. The ferrofluid flow is influenced by two magnets placed across a microchannel. The interacting field induced by these magnets promotes cross-stream motion of the ferrofluid, which induces its mixing with the other nonmagnetic fluid. Two fluids, one magnetic and another non-magnetic fluid, are

introduced in a channel, when two magnets are placed across it at a distance apart. In the presence of the magnetic field, the magnetic fluid tries to follow a zig-zag motion generating two rolls of vortices thereby enhancing mixing. A parametric study characterizes the effects of diffusivity, magnetic field strength, and relative magnet positions on a mixing parameter. Mixing is enhanced when the magnetic field strength and diffusivity are increased. However, contrary to the observed trend, placing the magnets very close to each other axially results in local ferrofluid agglomeration rather than promoting mixing.

This thesis is dedicated to my parents, Dr. Ramkrishna De and Mrs. Gita De and my brother Dr. Dibyendu De, without whose support, encouragement and inspiration it would never have been accomplished

ACKNOWLEDGEMENTS

I am grateful to my advisor Prof. Ishwar K. Puri for continuously inspiring me to approach new problems, overcome challenges and for allowing me the freedom to pursue something that was not even remotely related to his core research when I started. It was his unwavering support and faith in my work that helped me to successfully complete my research and made this challenging journey a smooth and memorable one. Prof. Puri has served as a true mentor – as much in my academic activities, as in the non-academic ones.

I extend sincere thanks to Prof. Mark Cramer and Prof. Hassan Aref for their suggestions and valuable advice. My sincere thanks to Prof. Michael Hyer and Prof. Mayuresh Patil for graciously agreeing to be on my thesis committee.

I thank Prof. Achintya Mukhopadhyay for the time and effort he put during my entire research. His contribution to this work has been enormous. I am also thankful to Prof. Swarnendu Sen and Dr. Ranjan Ganguly for their encouragement and support. I would also like to thank Mr. Tobias Rothaug, a diploma student from Germany, whom I mentored over Summer 2006. It was a very nice experience mentoring him, when he helped me immensely to parallelize my code.

The academic environment of Engineering Science and Mechanics Department has been very cordial. I have been lucky to be in the classes of a few outstanding teachers like Prof. Hassan Aref, Prof. Mark Cramer, Prof. David Dillard and Prof. Mayuresh Patil. I highly appreciate Prof. Romesh Batra and Prof. Muhammed Hajj's efforts to improve the graduate curriculum of the department. I have also enjoyed the out-of-the-class interactions with Prof. Hyer and various other faculty members of this department. At the same time, I would like to

thank all the staff members of the department for their great support, which made this journey a smooth one. All this directly or indirectly had salutary effects on my graduate study.

I would like to thank my friends, Soumik, Ashok, Sayan and Ganesh for their unconditional support in the lab as well as outside of it, even during my difficult times.

Finally I would like to thank those without whom I would never be able to accomplish anything – my parents and my brother.

AKD

TABLE OF CONTENT

LIST OF TABLES

LIST OF FIGURES

LIST OF FIGURES (Contd.)

LIST OF FIGURES (Contd.)

LIST OF FIGURES (Contd.)

NOMENCLATURE

$\mathbf{a}$	Force per unit mass (m/s^2)
a	Ferrofluid particle radius (m)
$\mathbf{B}$	Magnetic field (T)
c	Pseudo sonic speed (m/s)
c_s	Sonic speed (m/s)
D	Diffusivity (m^2/s)
$\mathbf{E}$	Electric field (V/m)
$\mathbf{e}$	Lattice speed (m/s)
e	Electric charge (1.602×10^{-19} C)
$\hat{\mathbf{e}}$	Unit vector
f	Probability density function
$\mathbf{H}$	$\mathbf{B}/\mu_0 - \mathbf{M}$
h	Channel height (m)
I	Shannon entropy index
k_B	Boltzmann constant (1.38×10^{23} J/K)
L	Length scale (m)
$\mathbf{M}$	Magnetization (A/m)
M	Mixing index
m	Dipole moment of line-dipole per unit length (A-m)
M_P	Magnetic pressure number
N	Number of particles

NOMENCLATURE (Contd.)

n	Number concentration (m^{-3})
p	Pressure (Pa)
$\mathbf{P}$	Pressure tensor (Pa)
Q	Collision integral
$\mathbf{R}$	Position vector of passive tracer particles (m)
R	Gas constant (J/kg-K)
Re	Reynolds number
$\mathbf{r}$	Position vector (m)
S	Shannon entropy
T	Absolute temperature
t	Time (s)
U	Velocity scale (m/s)
$\mathbf{u}$	Velocity vector (m/s)
u, v	Velocity (m/s)
W	Weight factor
w	Weight factor
x, y	Coordinates (m)
z	Valency

Greek and other symbols

α	Langevin parameter
ε	Permittivity of the medium (C/Vm)
Φ	Electric potential (V/m)

NOMENCLATURE (Contd.)

ϕ	Electric potential (V)
κ	Debye length (m)
μ	Viscosity (Pa-s)
μ_0	absolute permeability ($4\pi\times10^{-7}$ N/A^2)
ν	Kinematic viscosity (m^2/s)
θ	Polar coordinate (rad)
ρ	Density (kg/m^3)
σ	Mixing efficiency
τ	Relaxation time (s)
Ψ	Stream function (s^{-1})
ψ	Electric potential (V/m)
ζ	Zeta potential (V/m)

Subscripts and Superscripts

A, B	Species
e	Pertaining to electric
eq	Equilibrium
eff	Effective
sat	Saturation
α	Lattice direction
σ, *s*	Species
*	Normalized quantity

CHAPTER 1

INTRODUCTION

Microfluidic devices that allow for chemical reactions have a large number of sensor applications including multi-step chemical synthesis [1], bioanalytical diagnostics [2], DNA analysis [3], catalytic hydrogenation of alkenes [4], acid/base titrations [5], etc. Sensor miniaturization is driven by the need to reduce costs by reducing the consumption of reagents, decreasing analysis times, increasing the mixing efficiency and to enable automation. These needs, accompanied by the recent advancements in microfabrication technology have led to the development of micro-total analytical systems (μ-TAS) [6], more popularly known as *lab-on-a-chip* (*LOC*) devices. These devices have a relatively small size and are capable of performing the sample and reagent handling steps together with analytical measurements [7]. The importance of fluid mixing during complex chemical reactions cannot be overemphasized for *LOC* platforms. For instance, rapid mixing is essential in many microfluidic systems for proper biochemical analysis [8], sequencing or synthesis of nucleic acids [9], and for reproducible biological processes that involve cell activation [10], enzyme reactions [11], and protein folding [12].

1.1 Motivation

Flow residence time is effectively the average length of time that an entity, in this case a reagent molecule, will remain in a reactor. The limiting residence time governs the flow conditions through the control volume and is at most equal to the reaction time for the specified reacting species. At very small length scales, species transport in fluid flow

becomes dominated by molecular diffusion, which is usually very slow in comparison with the flow residence time at these scales. The slow mixing of reagents in microchannels often introduces a high degree of uncertainty about the starting time of the reaction [13]. In general, the chemical requirements in microfluidic devices can necessitate unacceptably long path lengths, e.g., ranging up to several millimeters for moderate flow rates (corresponding to velocities ~0.25-1 mm/s in 200 μm channels) [14,15].

Most miniaturized biochemical sensors and *LOC* devices developed thus far are steady-flow microfluidic devices that require relatively large sample and reactant volumes to ensure continuous flow. Achieving reasonably fast mixing is therefore a major challenge for microfluidic applications. Micromixers can either be integrated into these systems or can work as stand-alone devices. To induce active mixing (mixing dominated by modes other than diffusion alone), external energy input is required. Current modes of energy input utilize ultrasonic, acoustic and electrokinetic instabilities. Pulsed flow and physical impellers/valves are used for bigger channels. Integrated microfluidic platforms using additional devices and/or complex channeling are invasive to the microfluidic architecture and add complexity to system integration.

1.2 Background

Research on achieving better mixing in MEMS-scale devices has been ongoing. The mixing process is termed active or passive depending upon whether it calls for additional energy input (in addition to the pumping work) into the microscale flow. Both mixing types generate transverse flow components that either enhance mixing so that it is induced over relatively short distances [16] or create multilaminates [17].

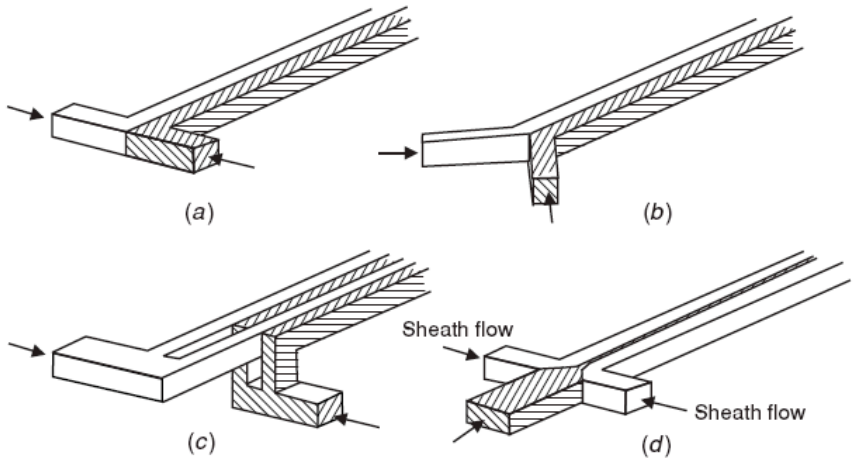

Figure 1.1. Parallel lamination micromixer: (*a*) the basic T-mixer and (*b*) Y-mixer, (*c*) the concept of parallel lamination and (*d*) the concept of hydraulic focusing.

1.2.1 Passive Mixers

Because of its simple concept, the passive mixer was one of the first microfluidic devices reported. Passive devices achieve mixing in a relatively simple manner, e.g., through the use of channels that are fabricated based on elaborate mixing designs [18,19]. These types of mixers are easier to integrate into *LOC* devices, but have lower mixing efficiencies than active systems, and require relatively large path lengths and more complicated structures. For instance, although three-dimensional serpentine passive mixers have been proven to have high mixing efficiencies [20], they require relatively long (~1 cm) path lengths and work best at high Reynolds numbers (>5) for channel dimensions of roughly 100-200 mm. One alternative is to create multiple (2-30) compact substream flows that intersect one another [16,18]. However, due to the small channel dimensions, the finer structures generating the substream flows must be patterned with a substantially higher resolution than for the channels themselves, which is problematic.

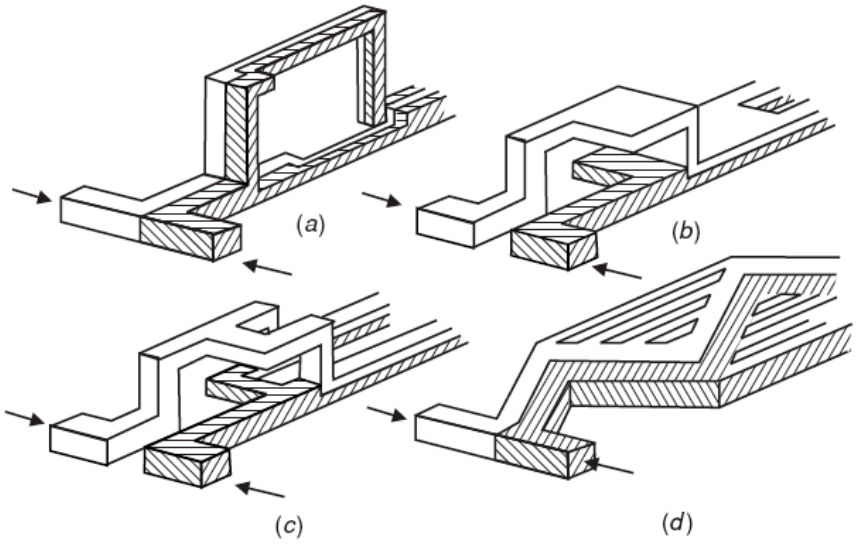

Figure 1.2. Serial lamination mixer: (*a*) join–split–join, (*b*) split–join [26], (*c*) split–split–join [29] and (*d*) multiple intersecting microchannels [30].

Parallel lamination micromixers

Fast mixing can be achieved by decreasing the mixing path and increasing the contact surface between the two phases. Parallel lamination splits the inlet streams into a number of substreams, then join them into one stream as laminae. The basic design is a long microchannel with two inlets to its geometry; these designs are often called the T-mixer or the Y-mixer [21 – 23] (Figs. 1.1*a* and *b*). Since the basic T-mixer entirely depends on molecular diffusion, a long mixing channel is needed. Besides the abovementioned concept of lamination of multiple streams, mixing at extremely high Reynolds numbers could also result in a short mixing length [24,25]. A chaotic flow is expected at these high Reynolds numbers. The induced vortices significantly enhance the mixing efficiency.

Serial lamination micromixer

Similar to parallel lamination micromixers, serial lamination micromixers also

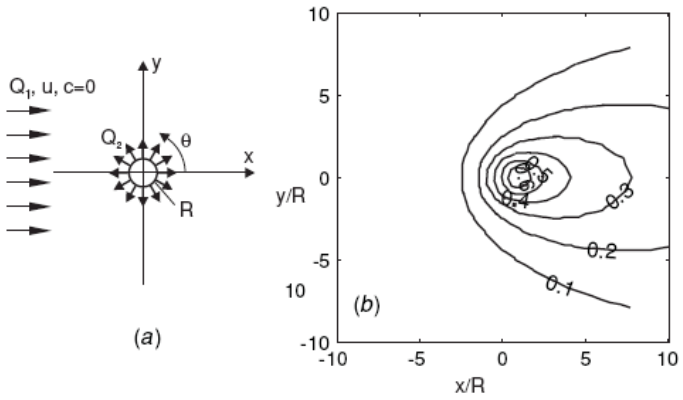

Figure 1.3. Injection mixer: (*a*) two-dimensional model and (*b*) typical dimensionless concentration distribution of a microplume (*Pe* = 1).

enhance mixing through splitting and later joining the streams as shown in Fig. 1.2 [26 – 29]. The inlet streams are first joined horizontally and then in the next stage vertically. After a number of splitting and joining stages, all the liquid layers created, can be laminated. The concept of the serial lamination micromixer can also be applied to electrokinetic flows as reported by He *et al* [30] (Fig. 1.2d). Using electro-osmosis flows between the multiple intersecting microchannels, mixing is clearly enhanced. A similar design for a pressure-driven flow was reported by Melin *et al* [31]. However, this design only works for a plug of the two mixed liquids.

Injection micromixers

The concept of the injection mixer [32 – 36] is similar to the parallel lamination mixer. Instead of splitting both inlet flows, this mixer type only splits the solute flow into many streams and injects them into the solvent flow. On top of one stream is an array of nozzles, which create a number of microplumes of the solute. These plumes increase the contact surface and decrease the mixing path. Mixing efficiency can be improved significantly. Figure 1.3 describes the two-dimensional model of the microplume from a

single circular nozzle of an injection mixer.

Micromixers based on chaotic advection

Besides diffusion, advection is another important form of mass transfer in flows with a low Reynolds number. However, advection is often parallel to the main flow direction, and is not useful for the transversal mixing process. The so-called chaotic advection can improve mixing significantly. Generally, chaotic advection can be generated by special geometries in the mixing channel or induced by an external force. The basic idea is the modification of the channel shape for splitting, stretching, folding and breaking of the flow. In the following, micromixers for different ranges of Reynolds number are discussed individually. Although there is no fixed range for a particular design, it is considered that the ranges $Re > 100$ as high, $10 < Re < 100$ as intermediate and $Re < 10$ as low.

Chaotic advection at high Reynolds number.

The simplest method to get chaotic advection is to insert obstacles structures in the mixing channel. Wang *et al* reported a numerical investigation of obstacles at high Reynolds numbers [37]. This work found that obstacles in a microchannel at low Reynolds numbers cannot generate eddies or recirculations (Fig. 1.4b). However, the results demonstrated that obstacles could improve mixing performance at high Reynolds numbers. Under this condition, the asymmetric arrangement of obstacles could alter the flow directions and force fluids to merge and create transversal mass transport. Lin *et al* [38] used cylinders placed in a narrow channel to enhance mixing. The next method to generate chaotic advection is using zig-zag microchannels to produce recirculation around the turns at high Reynolds numbers (Fig. 1.4c).

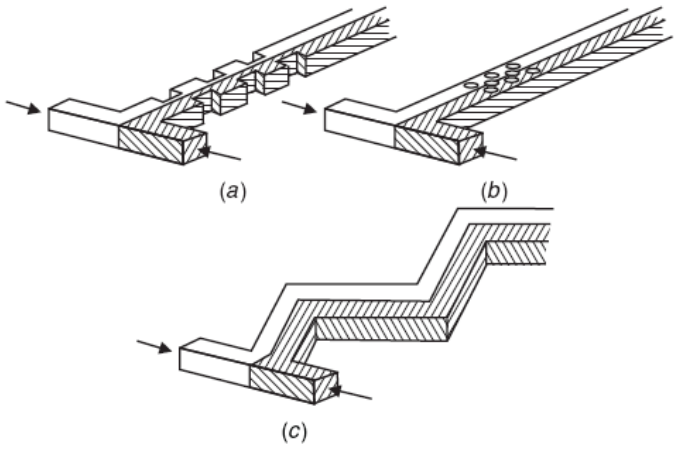

Figure 1.4. Planar designs for mixing with chaotic advection at high Reynolds numbers: (*a*) obstacles on wall, (*b*) obstacles in the channel [38] and (*c*) a zig-zag-shaped channel.

Chaotic advection at intermediate Reynolds numbers.

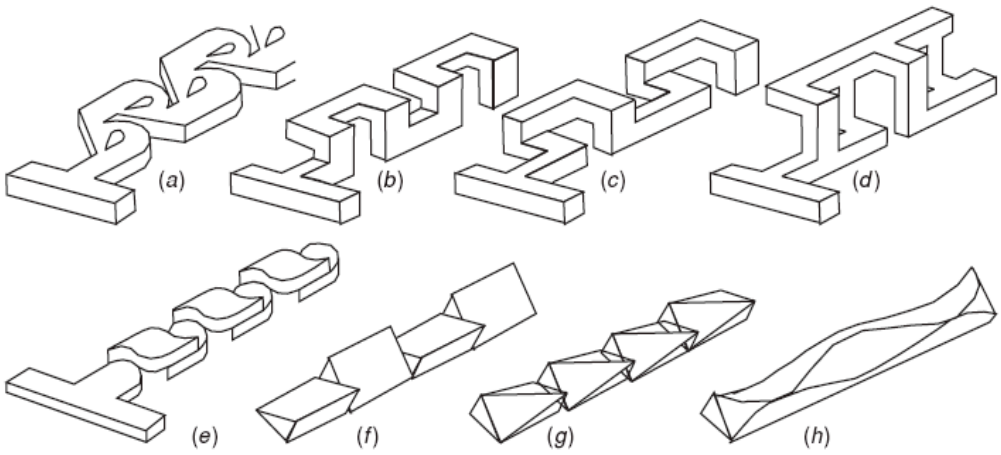

Figure 1.5. Micromixer designs for mixing with chaotic advection at intermediate Reynolds numbers: (*a*) modified Tesla structure, (*b*) C-shape [40], (*c*) L-shape, (*d*) connected out-of-plane L-shapes, (*e*) twisted microchannel and ((*f*), (*g*), (*h*)) other designs of twisted channel.

Hong *et al* [39] demonstrated an in-plane micromixer with two-dimensional modified Tesla structures. The Coanda effect in this structure causes chaotic advection and improves mixing significantly. Liu *et al* [40] reported a three-dimensional serpentine mixing channel constructed as a series of C-shaped segments positioned in perpendicular planes (Fig. 1.5b). The micromixer consists of two inlet channels joined in a T-junction, a straight channel and a sequence of six mixing segments. An interesting observation of the micromixer is that chaotic advection only occurs at relatively high Reynolds numbers (*Re* = 25–70) when the mixing process becomes faster. Figure 1.5 shows various other channel geometries that are designed to generating chaotic mixing at high Reynolds umber.

Chaotic advection at low Reynolds numbers.

Similar to macroscale mixers, rips or grooves on the channel wall can produce chaotic advection. Johnson *et al* [41] were the first to investigate this phenomenon. Almost at the same time, Stroock *et al* investigated this effect and published their results

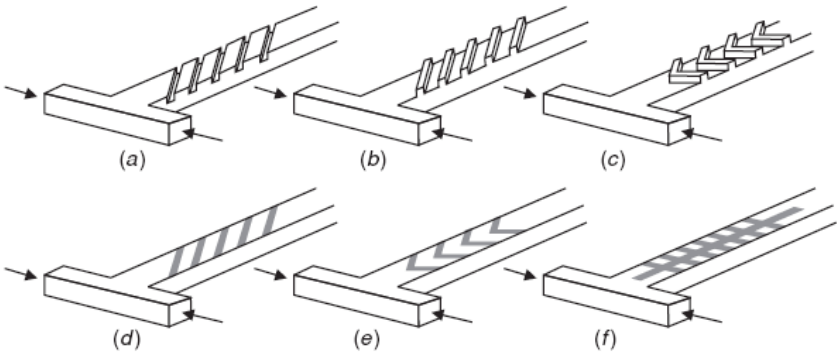

Figure 1.6. Modification of mixing channel for chaotic advection at low Reynolds numbers: (*a*) slanted ribs, (*b*) slanted grooves [42, 43], (*c*) staggered-herringbone grooves [42, 43] and (*d*)–(*f*) patterns for surface modification in a micromixer with electrokinetic flows.

in *Science* [42]. Two different groove patterns were considered. The so-called staggered herringbone mixer (Fig. 1.6c) can work well at a Reynolds number range from 1 to 10. This concept can be applied to electrokinetic flow by modifying the surface charge [43]. The effect of chaotic advection with the ripped channel was numerically investigated by Wang *et al* [44]. Kim *et al* [45] improved the design of Stroock *et al* [42] with embedded barriers parallel to the flow direction.

Droplet micromixers

Another solution for reducing the mixing path is to form droplets of the mixed liquids. The movement of a droplet causes an internal flow field and makes mixing inside the droplet possible. In general, droplets can be generated and transported individually using pressure [46] or capillary effects such as thermocapillary [47] and electrowetting [48]. Furthermore, droplets can be generated due to the large difference of surface forces in a small channel with multiple immiscible phases such as oil/water or water/gas [49]. Hosokawa et al [46] reported the earliest droplet micromixer. Handique and Burns reported an analytical model for droplet mixing actuated by thermocapillary [47]. Paik et al [48] reported different mixing schemes with the electrowetting concept. Droplets can be merged and split repeatedly to generate the mixing pattern. The merged droplet can then be transported around using electrowetting. The other droplet micromixer design used flow instability between two immiscible liquids [49,50]. Using a carrier liquid such as oil, droplets of the aqueous samples are formed. While moving through the microchannel, the shear force between the carrier liquid and the sample accelerated the mixing process in the droplet.

1.2.2 Active Mixers

Active devices have been based on rotating magnetic microbars that stir the flow [51], acoustic cavitation cells [52], electrokinetic instability [53], periodic flow switching [54], and pneumatically pumped rings [55]. These types of components require power and their mechanical construction can be quite complex. Hence, their integration into μ-TAS devices is challenging. Nonetheless, active devices can benefit from a simple "action-from-a-distance" solution that eliminates complexity and reduces the need to integrate a power supply into the microfabricated device.

Pressure field disturbance

Pressure field disturbance was used in one of the earliest active micromixers. Deshmukh *et al* [56] reported a T-mixer with pressure disturbance (Fig. 1.7a). The mixer is integrated in a microfluidic system. An integrated planar micropump drives and stops the flow in the mixing channel to divide the mixed liquids into serial segments and make the mixing process independent of convection. The performance of this micromixer was later discussed by Deshmukh *et al* in their other paper [57]. The pressure disturbance can also be generated by an external micropump [58]. Another alterative method to pressure disturbance is the generation of pulsing velocity [59,60] (Fig. 1.7*b*). Glasgow and Aubry [59] demonstrated a simple T-mixer and its simulation with a pulsed side flow at a small Reynolds number of 0.3. The paper did not elaborate further on the generation of the pulsed flow. In the work of Niu and Lee [60], the pressure disturbance was achieved by introducing a computer-controlled source–sink system. This design is partly similar to that of Evans *et al* [61]. The performance of the mixing process is related to the pulse frequency and the number of mixing units. A further modeling work on pressure

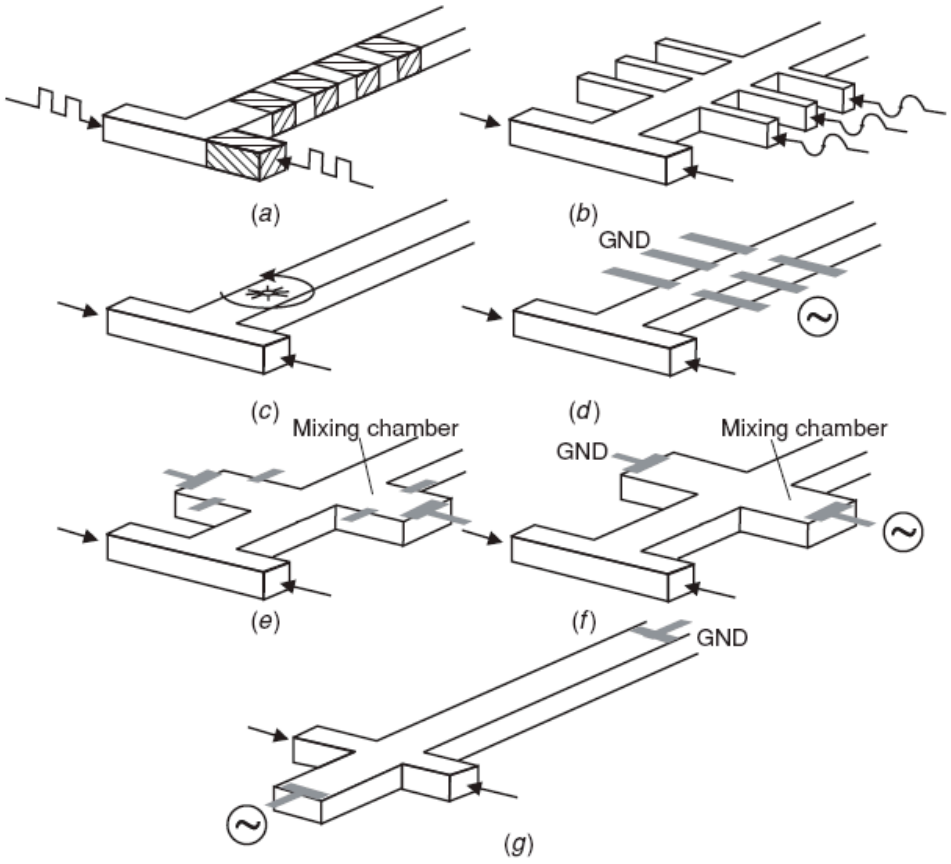

Figure 1.7. Active micromixers: (*a*) serial segmentation, (*b*) pressure disturbance along the mixing channel, (*c*) integrated microstirrer in the mixing channel, (*d*) electrohydrodynamic disturbance, (*e*) dielectrophoretic disturbance, (*f*) electrokinetic disturbance in the mixing chamber and (*g*) electrokinetic disturbance in the mixing channel.

disturbance was reported by Okkels and Tabeling [62]. However, the analysis focused only on the mixing pattern in the chamber.

Suzuki and Ho [63] reported a micromixer with integrated conductors. The electrical conductors generate a magnetic field, which in turn moves magnetic beads of 1–10 μm in diameter. The disturbance caused by the magnetic beads improves mixing

significantly. Disturbance can also be generated by an integrated magnetic microstirrer as reported by Lu *et al* [64]. The micromachined stirrer is placed at the interface between two liquids in a T-mixer. An external magnetic field drives the stirrer at a speed between 100 rpm and 600 rpm.

Electrohydrodynamic disturbance

The structure of the micromixer with eletrohydrodynamic disturbance [65] is similar to the concept reported by Niu and Lee [60]. Instead of pressure sources, electrodes are placed along the mixing channel (Fig. 1.7d). A series of titanium wires is placed in the direction perpendicular to the mixing channel. By changing the voltage and frequency on the electrodes good mixing was achieved after less than 0.1 s at a low Reynolds number of 0.02.

Dielectrophoretic disturbance

Dielectrophoresis (DEP) is the polarization of a particle relatively to its surrounding medium in a non-uniform electrical field. This effect causes the particle to move to and from an electrode. Deval *et al* [66] and Lee *et al* [67] reported a dielectrophoretic micromixer (Fig. 1.7e). Chaotic advection was generated by embedded particles with a combination of electrical actuation and local geometry channel variation.

Electrokinetic disturbance

Electrokinetic flow can be used to transport liquid in micromixers as an alternative to pressure driven flow. Jacobson *et al* [68] reported electrokinetically driven mixing in a conventional T-mixer. Lettieri *et al* proposed the use of the electrokinetic effect to disturb the pressure-driven flow in a micromixer [69]. In another case [70], oscillating electro-osmotic flow in a mixing chamber is caused by an ac voltage. The

pressure-driven flow becomes unstable in a mixing chamber (Fig. 1.7f) or in a mixing channel (Fig. 1.7g). Tang *et al* also utilized an electrokinetic flow to improve mixing [71]. Similar to the previous pressure-driven approach [56], switching on or off the voltage supplied to the flow generates fluid segments in the mixing channel. This flow modulation scheme was capable of injecting reproducible and stable fluid segments into microchannels at a frequency between 0.01 Hz and 1 Hz.

Magneto hydrodynamic disturbance

The magneto hydrodynamic effect [72] has been used in micromixers. In the presence of an external magnetic field applied dc voltages on the electrodes generate Lorentz forces, which in turn can induce roll and fold of the liquids in a mixing chamber. This concept only works with an electrolyte solution.

Acoustic disturbance

Acoustic actuators were used to stir fluids in micromixers. The proof of concept for acoustic mixing was reported by Moroney *et al* [73] with a flexible-plate-wave (FPW) device. Zhu and Kim [74] gave an analysis of the focused acoustic wave model in a mixing chamber. The vibration can be controlled by changing the frequency and the voltage of the input signal. The concept of acoustically induced flow, or acoustic streaming, was also used as an active mixing scheme [75]. Focused acoustic streaming with different electrode patterns was used for mixing [76]. Besides the integrated design, stirring at high frequency can also be realized by an external pump [77]. Ultrasonic mixing may have problems in applications for biological and chemical analysis because of the temperature rise caused by acoustic energy. Many biological fluids are highly sensitive to temperature. Furthermore, ultrasonic waves around 50 kHz are harmful to

biological samples because of the possible cavitations. The acoustic micromixer reported by Yasuda [78] used loosely focused acoustic waves to generate stirring movements. The mixer operated without any significant temperature increase and could be used for temperature-sensitive fluids. Further acoustic devices for mixing water and ethanol as well as water and uranine were reported by Yang *et al* [79,80]. Liu *et al* [81,82] used acoustic streaming induced around an air bubble for mixing. Yaralioglu *et al* [83] also utilized acoustic streaming to disturb the flow in a conventional Y-mixer.

Thermal disturbance

Since the diffusion coefficient depends highly on temperature, thermal energy can also be used to enhance mixing [84,85]. Mao *et al* [84] generated a linear temperature gradient across a number of parallel channels in order to investigate the temperature dependence of fluorescent dyes. This approach can possibly be used for micromixing. The other design [85] utilized a thermal bubble to generate disturbance in a mixing channel.

1.3 Objective

The salient objective of the thesis is to study the effect of different body forces on the fluid flow and thereby enhance microscale mixing. The study involves two mixing schemes, namely, electroosmotic mixing and magnetic assisted mixing.

In contrast to the earlier studies, which relied on either unsteady flows or complex potential distributions, we present a relatively simpler scheme to achieve rapid mixing that uses a steady electric potential and a homogeneous zeta potential in an easily implemented cavity configuration. A single component LBM model is developed to study electroosmotic flow in a square cavity. A Boltzmann equation is solved analytically to

determine the charge as well as potential distribution inside the square cavity. The fluid flow is solved by resolving the electric double layer (EDL) formed close to the cavity wall, instead of following the common practice of applying slip velocity at the wall. The mixing is studied by introducing two kinds of passive tracer particles in the steady electroosmotic flow. The mixing is characterized by using various mixing parameters.

A multicomponent 2-D LBM method is developed to study magnetic assisted mixing in a channel configuration. Two fluids, one magnetic and another non-magnetic fluid, are introduced in a channel, when two magnets are placed across it at an axial distance apart. The magnets are modeled as line dipoles. In presence of the interacting magnetic fields, ferrofluid tries to follow a zig-zag motion and generates two rolls of vortices which enhances mixing. The mixing is charaterized by using the parameter mixing index. The effect of diffusivity, strength of magnetic field, and position of magnet relative to the channel and relative to each other is studied. Specifically, the study presented in this thesis pursues the following tasks.

1.3.1 Electroosmotic Mixing

- Solve the Boltzmann equation analytically to obtain the electric charge distribution in the cavity as well as the potential distribution.
- Develop a fully parallelized numerical code using a lattice Boltzmann method, validated against the standard benchmark solution, to model the electroosmotic flow.
- Study the mixing in a cavity configuration by using steady electric field and homogeneous zeta potential.

- Characterize mixing by introducing two kinds of passive tracer particles in the steady electroosmotic flow and using various mixing parameters.

1.3.2 Magnetic Assisted Mixing

- Develop a numerical model using two-dimensional multicomponent lattice Boltzmann method to capture the ferrohydrodynamic flow.
- Predict the flow and mixing of two fluids, one of which is a magnetic fluid, in presence of two magnets placed across the channel at an axial distance apart.
- Characterize mixing by using a mixing parameter.
- Study the effect of diffusivity, magnetic field strength and theirs placement relative to each other as well as relative to the channel on the microscale mixing.

CHAPTER 2

LATTICE BOLTZMANN METHOD

2.1 Background

Lattice Boltzmann method (LBM) is a relatively new simulation technique for complex fluid systems and has attracted interest from researchers in computational physics. Unlike the traditional CFD methods, which solve the conservation equations of macroscopic properties (i.e., mass, momentum, and energy) numerically, LBM models the fluid consisting of fictitious particles, and such particles perform consecutive propagation and collision processes over a discrete lattice mesh. Due to its particulate nature and local dynamics, LBM has several advantages over other conventional CFD methods, especially in dealing with complex boundaries, incorporating of microscopic interactions, and parallelization of the algorithm. In recent years, the lattice Boltzmann method (LBM) has developed into an alternative and promising numerical scheme for simulating fluid flows and modeling physics in fluids. The scheme is particularly successful in fluid flow applications involving interfacial dynamics and complex boundaries.

LBM originated from the Lattice Gas Automata (LGA) method, which can be considered as a simplified fictive molecular dynamics model in which space, time, and particle velocities are all discrete. Each lattice node is connected to its neighbors by 6 lattice velocities, using for example the hexagonal FHP model. There can be either 0 or 1 particle at a lattice node moving in a lattice direction. After a time interval, each particle will move to the neighboring node in its direction, this process is called the propagation

or streaming step. When there are more than one particles arriving at the same node from different directions, they collide and change their directions according to a set of collision rules. Suitable collision rules should conserve the particle number (mass), momentum, and energy before and after the collision. However, it was found that LGA suffers from several native defects: lack of Galilean invariance, statistical noise, and exponential complexity for three-dimensional lattices, to name a few.

The main motivation for the transition from LGA to LBM was the desire to remove the statistical noise by replacing the Boolean particle number in a lattice direction with its ensemble average, the so-called density distribution function. Accompanying this replacement, the discrete collision rule is also replaced by a continuous function known as the collision operator. In the LBM development, an important simplification is to approximate the collision operator with the Bhatnagar-Gross-Krook (BGK) relaxation term. This lattice BGK (LBGK) model makes simulations more efficient and allows flexibility of the transport coefficients. On the other hand, it has been shown that the LBM scheme can also be considered as a special discretized form of the continuous Boltzmann equation. Through a Chapman-Enskog analysis, one can recover the governing continuity and Navier-Stokes equations from the LBM algorithm. In addition, the pressure field is also directly available from the density distributions and hence there is no extra Poisson equation to be solved as in traditional CFD methods.

At the macroscopic scale, matter is treated as continuum and the dynamic behaviour is described by a system of partial differential equations (PDEs). The form of these PDEs does not depend on the microscopic details. Conventional CFD techniques are based on discretization of these PDEs. On the other hand, at the microscopic level

discrete atoms or molecules build up any fluid. A trivial way to simulate small-scale fluid systems is to follow the movement and collisions of a large number of individual molecules. This approach is called molecular dynamics (MD). MD cannot be used for large- or medium-scale simulations, since it would need extremely large computational resources. In between these approaches, a third approach involves reducing the computational requirements by reducing the degree of freedom of the system, e.g. by forcing the movement of the molecules to a lattice. In this approach, instead of individual molecules attention is focused on groups of molecules. Consequently these methods are often called mesoscopic ones. Lattice Boltzmann Method (LBM) falls in this category. Being mesoscopic in nature, on one hand it can handle reasonably large-scale systems and at the same time it can capture many small scale phenomena. Recent advances on LBM have been reviewed by Chen and Doolen [86], Hazi et al. [87], Yu et al. [88] and Nourgaliev et al. [89].

Unlike conventional numerical schemes based on discretizations of macroscopic continuum equations, the lattice Boltzmann method is based on microscopic models and mesoscopic kinetic equations. The fundamental idea of the LBM is to construct simplified kinetic models that incorporate the essential physics of microscopic or mesoscopic processes so that the macroscopic averaged properties obey the desired macroscopic equations. Even though the LBM is based on a particle picture, its principal focus is the averaged macroscopic behavior. The kinetic equation provides many of the advantages of molecular dynamics, including clear physical pictures, easy implementation of boundary conditions, and fully parallel algorithms. The kinetic nature of the LBM introduces three important features that distinguish it from other numerical

methods [86]. First, the convection operator (or streaming process) of the LBM in phase space (or velocity space) is linear. This feature is borrowed from kinetic theory and contrasts with the nonlinear convection terms in other approaches that use a macroscopic representation. Simple convection combined with a relaxation process (or collision operator) allows the recovery of the nonlinear macroscopic advection through multi-scale expansions. Second, the incompressible Navier-Stokes (NS) equations can be obtained in the nearly incompressible limit of the LBM. The pressure of the LBM is calculated using an equation of state. In contrast, in the direct numerical simulation of the incompressible NS equations, the pressure satisfies a Poisson equation with velocity strains acting as sources. Solving this equation for the pressure often produces numerical difficulties requiring special treatment, such as iteration or relaxation. Third, the LBM utilizes a minimal set of velocities in phase space. In the traditional kinetic theory with the Maxwell-Boltzmann equilibrium distribution, the phase space is a complete functional space. The averaging process involves information from the whole velocity phase space. Because only one or two speeds and a few moving directions are used in LBM, the transformation relating the microscopic distribution function and macroscopic quantities is greatly simplified and consists of simple arithmetic calculations.

2.2 Boltzmann Equation

Although historically Lattice Boltzmann Method evolved from Lattice Gas Automata (LGA), an alternative and a more elegant interpretation of LBM is obtained by considering the Boltzmann equation directly [88,89]. The primary variable of interest in Boltzmann equation is the particle probability distribution function, $f(\mathbf{r},\mathbf{e},t)$ defined

such that $f(\mathbf{r},\mathbf{e},t)d^3\mathbf{r}d^3\mathbf{e}$ denotes the number of particles within the phase space control volume $d^3\mathbf{r}d^3\mathbf{e}$ centered around the position, **r** and velocity, **e** of the particle. The general form of Boltzmann equation is [90]

$$\frac{\partial f}{\partial t} + \mathbf{e}\cdot\nabla_{\mathbf{r}} f + \mathbf{a}\cdot\nabla_{\mathbf{e}} f = \left(\frac{\partial f}{\partial t}\right)_{scat} \tag{2.1}$$

In Eq. (2.1), the second term on LHS denotes the streaming or the advection term. The third term on LHS denotes the contribution of the force **a** acting on the particle. The RHS of Eq. (2.1) denotes the rate of change of the distribution due to collision or scattering. This term restores equilibrium. The collision term needs to be explicitly specified. However, it can be considerably simplified for non-equilibrium states using "collision interval theory". The collision interval theory states that during an interval δt, a fraction $1/\tau'$ of the particles in a given small volume undergoes collisions, which alter the PDF from f to f_{eq}. Thus, due to scattering, change in number of particles in the volume element $d^3\mathbf{r}d^3\mathbf{e}$ in time δt is $\frac{1}{\tau'}(f - f_{eq})$. Thus $\left(\frac{\partial f}{\partial t}\right)_{scat} = -\frac{(f - f_{eq})/\tau'}{\delta t} = -\frac{f - f_{eq}}{\tau}$, where $\tau = \tau'\delta t$ is called a relaxation time. The above simplification of the scattering term is known as single relaxation time (SRT) or Bhatnagar-Gross-Krook (BGK) approximation. It may be noted that alternative formulations based on multiple relaxation time (MRT) approximations are also available and often used for handling multifluid or multicomponent systems [91,92]. The Boltzmann equation with BGK approximation becomes

$$\frac{\partial f}{\partial t} + \mathbf{e}\cdot\nabla_{\mathbf{r}} f + \mathbf{a}\cdot\nabla_{\mathbf{e}} f = -\frac{f - f_{eq}}{\tau(\mathbf{r},\mathbf{e})} \tag{2.2}$$

This form effectively linearizes the Boltzmann equation. It also implies that if a system is thrown out of equilibrium, equilibrium is restored following an exponential decay i.e., $f - f_{eq} \approx \exp(-t/\tau)$. For small deviations from equilibrium, $\nabla_{\mathbf{e}} f \approx \nabla_{\mathbf{e}} f_{eq}$. The distribution, f_{eq} is generally Maxwell-Boltzmann for gas molecules i.e.,

$$f_{eq} = \frac{\rho}{(2\pi RT)^{L/2}} \exp\left[-\frac{(\mathbf{e}-\mathbf{u})^2}{2RT}\right] \tag{2.3}$$

In the above equation, ρ, R, T, L and **u** represent macroscopic density, gas constant, macroscopic temperature, characteristic length and macroscopic gas velocity respectively. Thus for Maxwellian distribution, $\nabla_{\mathbf{e}} f \approx \nabla_{\mathbf{e}} f_{eq} = \frac{\mathbf{e}-\mathbf{u}}{RT} f_{eq}$. Thus

$$\frac{\partial f}{\partial t} + \mathbf{e}\cdot\nabla_{\mathbf{r}} f = -\frac{f - f_{eq}}{\tau(\mathbf{r},\mathbf{e})} + \frac{\mathbf{a}\cdot(\mathbf{e}-\mathbf{u})}{RT} f_{eq} \tag{2.4}$$

The equilibrium distribution, f_{eq} is given by

$$f_{eq} = \frac{\rho}{(2\pi RT)^{L/2}} \exp\left[-\frac{\mathbf{e}\cdot\mathbf{e}}{2RT} + \frac{\mathbf{e}\cdot\mathbf{u}}{RT} - \frac{\mathbf{u}\cdot\mathbf{u}}{2RT}\right] = \frac{\rho}{(2\pi RT)^{L/2}} \exp\left(-\frac{\mathbf{e}\cdot\mathbf{e}}{2RT}\right)\left[1 + \frac{\mathbf{e}\cdot\mathbf{u}}{RT} + \frac{1}{2}\left(\frac{\mathbf{e}\cdot\mathbf{u}}{RT}\right)^2 - \frac{\mathbf{u}\cdot\mathbf{u}}{2RT}\right] \tag{2.5}$$

The equilibrium distribution given by Eq. (2.5) is known as Low Mach Number Approximation (LMNA). The macroscopic variables like density and momentum are hydrodynamic moments of the distribution function $\rho = \int f d\mathbf{e}$ and $\rho\mathbf{u} = \int f \mathbf{e} d\mathbf{e}$.

2.3 Discretized Boltzmann Equation

To obtain the discretized form of Boltzmann equation, we first neglect the force term. Neglecting the last term, Eq. (2.4), can be expressed as an ODE in the following form:

$$\frac{df}{dt} + \frac{f}{\tau} = \frac{f_{eq}}{\tau} \tag{2.6}$$

where $\frac{d}{dt} \equiv \frac{\partial}{\partial t} + \mathbf{e} \cdot \nabla$ is the time derivative along the characteristic direction, **e**. Eq. (2.6) can be formally integrated over a time step δt as [93]

$$f(\mathbf{r} + \mathbf{e}\delta t, \mathbf{e}, t + \delta t) = \frac{1}{\tau} e^{-\delta t/\tau} \int_0^{\delta t} e^{t'/\tau} f_{eq}(\mathbf{r} + \mathbf{e}t', \mathbf{e}, t + t') dt' + e^{-\delta t/\tau} f(\mathbf{r}, \mathbf{e}, t) \tag{2.7}$$

Linear interpolation gives

$$f_{eq}(\mathbf{r} + \mathbf{e}t', \mathbf{e}, t + t') = f_{eq}(\mathbf{r}, \mathbf{e}, t) + \frac{t'}{\delta t}\left[f_{eq}(\mathbf{r} + \mathbf{e}\delta t, \mathbf{e}, t + \delta t) - f_{eq}(\mathbf{r}, \mathbf{e}, t) \right]$$

Substituting the above in Eq. (2.7) gives

$$f(\mathbf{r} + \mathbf{e}\delta t, \mathbf{e}, t + \delta t) - f(\mathbf{r}, \mathbf{e}, t) = \left(e^{-\delta t/\tau} - 1\right)\left[f(\mathbf{r}, \mathbf{e}, t) - f_{eq}(\mathbf{r}, \mathbf{e}, t) \right] + \left\{ 1 + \frac{\tau}{\delta t}\left(e^{-\delta t/\tau} - 1\right) \right\}\left[f_{eq}(\mathbf{r} + \mathbf{e}\delta t, \mathbf{e}, t + \delta t) - f_{eq}(\mathbf{r}, \mathbf{e}, t) \right] \tag{2.8}$$

Noting that $1 + \frac{\tau}{\delta t}\left(e^{-\delta t/\tau} - 1\right) = 1 + \frac{\tau}{\delta t}\left(1 - \frac{\delta t}{\tau} + O(\delta t^2) - 1\right) = O(\delta t^2)$ and $e^{-\delta t/\tau} - 1 = -\frac{\delta t}{\tau} + O(\delta t^2)$ and neglecting $O(\delta t^2)$ terms, Eq. (2.7) becomes

$$f(\mathbf{r} + \mathbf{e}\delta t, \mathbf{e}, t + \delta t) - f(\mathbf{r}, \mathbf{e}, t) = -\frac{\delta t}{\tau}\left[f(\mathbf{r}, \mathbf{e}, t) - f_{eq}(\mathbf{r}, \mathbf{e}, t) \right] \tag{2.9}$$

The discretized Boltzmann equation then becomes

$$f(\mathbf{r} + \mathbf{e}\delta t, \mathbf{e}, t + \delta t) - f(\mathbf{r}, \mathbf{e}, t) = -\frac{1}{\tau^*}\left[f(\mathbf{r}, \mathbf{e}, t) - f_{eq}(\mathbf{r}, \mathbf{e}, t) \right] \tag{2.10}$$

where $\tau^* = \tau / \delta t$ is the dimensionless relaxation time. In Lattice Boltzmann method, Eq. (2.2) is discretized in the velocity space using a finite set of velocity vectors $\{\mathbf{e}_\alpha\}$. The completely discretized equation, with time step, δt and space step, $\delta \mathbf{r} = \mathbf{e}_\alpha \delta t$ becomes

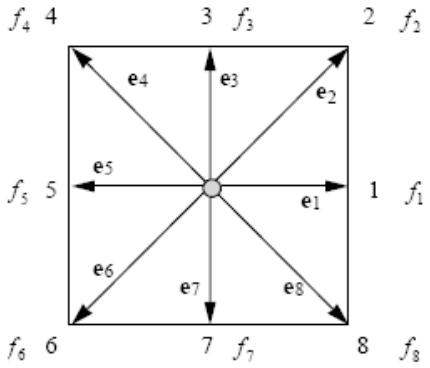

Figure 2.1. A 2-D 9-velocity (D2Q9) model.

$$f_\alpha(\mathbf{r}_i + \mathbf{e}_\alpha \delta t, t + \delta t) - f_\alpha(\mathbf{r}_i, t) = -\frac{1}{\tau^*}\left[f_\alpha(\mathbf{r}_i, t) - f_{eq,\alpha}(\mathbf{r}_i, t)\right] \tag{2.11}$$

where $\mathbf{r}_i$ is a point in the discretized physical space. Equation (2.11) is the discretized Boltzmann equation on a lattice space or Lattice Boltzmann equation (LBE). In the above equation, $f_\alpha(\mathbf{r}_i, t) \equiv f(r, e_\alpha, t)$ is the f distribution corresponding to α^{th} discrete velocity $\mathbf{e}_\alpha$ and f_α^{eq} is the corresponding equilibrium distribution in the discrete velocity space. The most popular lattice model for 2-D configurations is the 2-D 9-velocity (D2Q9) model (Fig. 2.1). For D2Q9 model, the discrete velocities are given by

$$\mathbf{e}_\alpha = (0,0),\ \alpha = 0;\quad c\left\{\cos(\alpha-1)\frac{\pi}{4},\ \sin(\alpha-1)\frac{\pi}{4}\right\},\ \alpha = 1,3,5,7;\quad \sqrt{2}c\left\{\cos(\alpha-1)\frac{\pi}{4},\ \sin(\alpha-1)\frac{\pi}{4}\right\},\ \alpha = 2,4,6,8$$

In the above expressions, c is given by $c = \delta x / \delta t$ and is related to speed of sound, c_s as $c_s^2 = \frac{c^2}{3} = \frac{p}{\rho} = RT$ (for ideal gas). In terms of discrete velocities, the integrals in the evaluation of macroscopic variables are replaced by quadratures: $\rho = \sum_\alpha W_\alpha f_\alpha$ and $\rho \mathbf{u} = \sum_\alpha W_\alpha f_\alpha \mathbf{e}_\alpha$.

Using $W_\alpha f_\alpha$ as the effective distribution function in discrete velocity space, one can substitute the effective distribution in Eq. (2.5) and obtain the equilibrium distribution as

$$f_\alpha^{eq} = \rho w_\alpha \left[1 + \frac{3}{c^2}\mathbf{e}_\alpha \cdot \mathbf{u} + \frac{9}{2c^4}(\mathbf{e}_\alpha \cdot \mathbf{u})^2 - \frac{3}{2c^2}\mathbf{u}\cdot\mathbf{u}\right] \tag{2.12}$$

The weights in Eq. (2.12) are $w_\alpha = \frac{W_\alpha}{(2\pi RT)^{L/2}} \exp\left(-\frac{3\mathbf{e}\cdot\mathbf{e}}{2c^2}\right)$ and given by

$$w_\alpha = \frac{4}{9},\ \alpha = 0; \quad \frac{1}{9}, \quad \alpha = 1,3,5,7; \quad \frac{1}{36}, \quad \alpha = 2,4,6,8$$

The details of the procedure for calculation of these weights can be found in [93].

2.3.1 Derivation of Transport Equations

Before discussing the numerical implementation of LBM, we would show the relation between the Boltzmann equation and the macroscopic transport equations. The macroscopic parameters like density and velocity are obtained as moments of the distribution function, *f*. Expanding $f_\alpha(\mathbf{r} + \mathbf{e}_\alpha \Delta t, t + \Delta t)$ in Taylor's series in Eq. (2.11) [94,95]

$$\left(\frac{\partial}{\partial t} + \mathbf{e}_\alpha \cdot \nabla\right) f_\alpha \delta t + \frac{1}{2}\left(\frac{\partial}{\partial t} + \mathbf{e}_\alpha \cdot \nabla\right)^2 f_\alpha (\delta t)^2 + O(\delta t)^3 = -\frac{f_\alpha - f_\alpha^{eq}}{\tau^*} \tag{2.13}$$

To derive the hydrodynamic moments, we apply a formal multiscale approximation, known as Chapman-Enskog expansion as follows:

$t = t_0 + \frac{t_1}{\varepsilon};\ \mathbf{r} = \mathbf{r}_0$. Thus,

$$\frac{\partial}{\partial t} = \frac{\partial}{\partial t_0} + \varepsilon \frac{\partial}{\partial t_1};\ \ \nabla = \nabla_0 \tag{2.14}$$

where $\nabla \equiv \frac{\partial}{\partial \mathbf{r}};\ \nabla_0 \equiv \frac{\partial}{\partial \mathbf{r}_0}; \varepsilon = \delta t$.

We expand $f_\alpha(\mathbf{r},t) = \sum_{n=0}^{\infty} \varepsilon^n f_\alpha^{(n)}(\mathbf{r},t) = f_\alpha^{(0)}(\mathbf{r},t) + \varepsilon f_\alpha^{(1)}(\mathbf{r},t) + \varepsilon^2 f_\alpha^{(2)}(\mathbf{r},t) + \ldots$ (2.15)

subject to the constraints

$$\sum_{\alpha} w_\alpha f_\alpha^{(0)} \begin{Bmatrix} 1 \\ \mathbf{e}_\alpha \end{Bmatrix} = \begin{Bmatrix} \rho \\ \rho \mathbf{u} \end{Bmatrix} \text{ and } \sum_{\alpha} w_\alpha f_\alpha^{(n)} \begin{Bmatrix} 1 \\ \mathbf{e}_\alpha \end{Bmatrix} = \begin{Bmatrix} 0 \\ \mathbf{0} \end{Bmatrix}, \text{ n} \geq 1 \tag{2.16}$$

Substituting Eqs. (2.14) and (2.15) in Eq. (2.13), we obtain

$$\left[\varepsilon \left\{ \frac{\partial}{\partial t_0} + \varepsilon \frac{\partial}{\partial t_1} + \mathbf{e}_\alpha \cdot \nabla_{\mathbf{0}} \right\} + \frac{\varepsilon^2}{2} \left\{ \frac{\partial}{\partial t_0} + \varepsilon \frac{\partial}{\partial t_1} + \mathbf{e}_\alpha \cdot \nabla_{\mathbf{0}} \right\}^2 \right] \left\{ f_\alpha^{(0)}(\mathbf{r},t) + \varepsilon f_\alpha^{(1)}(\mathbf{r},t) + \varepsilon^2 f_\alpha^{(2)}(\mathbf{r},t) + ... \right\} \tag{2.17}$$
$$= -\frac{f_\alpha^{(0)}(\mathbf{r},t) + \varepsilon f_\alpha^{(1)}(\mathbf{r},t) + \varepsilon^2 f_\alpha^{(2)}(\mathbf{r},t) - f_{eq,\alpha}(\mathbf{r},t)}{\tau^*}$$

Collecting coefficients of different powers of ε ,

$$\varepsilon^0 : f_\alpha^{(0)}(\mathbf{r},t) = f_{eq,\alpha}(\mathbf{r},t) \tag{2.18a}$$

$$\varepsilon^1 : \frac{\partial f_\alpha^{(0)}}{\partial t_0} + \mathbf{e}_\alpha \cdot \nabla_0 f_\alpha^{(0)} = -\frac{f_\alpha^{(1)}}{\tau^*} \tag{2.18b}$$

$$\varepsilon^2 : \frac{\partial f_\alpha^{(0)}}{\partial t_1} + \left(\frac{\partial}{\partial t_0} + \mathbf{e}_\alpha \cdot \nabla_0 \right) f_\alpha^{(1)} + \frac{1}{2} \left(\frac{\partial}{\partial t_0} + \mathbf{e}_\alpha \cdot \nabla_0 \right)^2 f_\alpha^{(0)} = -\frac{f_\alpha^{(2)}}{\tau^*}$$

Using Eq. (2.18b) we can write the above equation as

$$\frac{\partial f_\alpha^{(0)}}{\partial t_1} + \left(1 - \frac{1}{2\tau^*} \right) \left(\frac{\partial}{\partial t_0} + \mathbf{e}_\alpha \cdot \nabla_0 \right) f_\alpha^{(1)} = -\frac{f_\alpha^{(2)}}{\tau^*} \tag{2.18c}$$

Multiplying Eq. (2.18b) by w_α and summing over all directions (noting that $\mathbf{e}_\alpha \cdot \nabla_0 f_\alpha^{(0)} = \nabla_0 \cdot \left(\mathbf{e}_\alpha f_\alpha^{(0)} \right)$ since $\mathbf{e}_\alpha$ is independent of $\mathbf{r}$)

$$\frac{\partial}{\partial t_0} \sum_\alpha w_\alpha f_\alpha^{(0)} + \nabla_0 \cdot \left(\sum_\alpha \mathbf{e}_\alpha w_\alpha f_\alpha^{(0)} \right) = -\frac{\sum_\alpha w_\alpha f_\alpha^{(1)}}{\tau^*}$$

From the constraints in Eq. (2.16),

$$\frac{\partial \rho}{\partial t_0} + \nabla_0 \cdot (\rho \mathbf{u}) = 0 \tag{2.19}$$

Eq. (2.19) is the equation for conservation of mass.

Multiplying Eq. (2.18b) by $w_\alpha \mathbf{e}_\alpha$ and summing over all directions,

$$\frac{\partial}{\partial t_0}\sum_\alpha w_\alpha \mathbf{e}_\alpha f_\alpha^{(0)} + \nabla_0 \cdot \left(\sum_\alpha \mathbf{e}_\alpha \mathbf{e}_\alpha w_\alpha f_\alpha^{(0)}\right) = -\frac{\sum_\alpha w_\alpha \mathbf{e}_\alpha f_\alpha^{(1)}}{\tau^*}$$

We expand the second term in the above equation as

$$\begin{aligned}\sum_\alpha \mathbf{e}_\alpha \mathbf{e}_\alpha w_\alpha f_\alpha^{(0)} &= \sum_\alpha \{(\mathbf{e}_\alpha - \mathbf{u}) + \mathbf{u}\}\{(\mathbf{e}_\alpha - \mathbf{u}) + \mathbf{u}\} w_\alpha f_\alpha^{(0)} \\ &= \sum_\alpha (\mathbf{e}_\alpha - \mathbf{u})(\mathbf{e}_\alpha - \mathbf{u}) w_\alpha f_\alpha^{(0)} + \mathbf{uu}\sum_\alpha w_\alpha f_\alpha^{(0)} + 2\mathbf{u}\sum_\alpha w_\alpha \mathbf{e}_\alpha f_\alpha^{(0)} - 2\mathbf{uu}\sum_\alpha w_\alpha f_\alpha^{(0)}\end{aligned}$$

Using the constraints in Eq. (2.16) and introducing the nth approximation of pressure tensor as $\mathbf{P}^{(n)} = \sum_\alpha (\mathbf{e}_\alpha - \mathbf{u})(\mathbf{e}_\alpha - \mathbf{u}) w_\alpha f_\alpha^{(n)}$ we get,

$$\frac{\partial}{\partial t_0}(\rho \mathbf{u}) + \nabla_0 \cdot (\rho \mathbf{uu}) = -\nabla_0 \cdot \mathbf{P}^{(0)} \tag{2.20}$$

Multiplying each term of Eq. (2.18c) by w_α and summing and using the constraints in Eq. (2.15), we get

$$\frac{\partial \rho}{\partial t_1} = 0 \tag{2.21}$$

Multiplying each term of Eq. (2.18c) by $w_\alpha \mathbf{e}_\alpha$ and summing

$$\frac{\partial}{\partial t_1}\sum_\alpha w_\alpha \mathbf{e}_\alpha f_\alpha^{(0)} + \left(1 - \frac{1}{2\tau^*}\right)\left(\frac{\partial}{\partial t_0}\sum_\alpha w_\alpha \mathbf{e}_\alpha f_\alpha^{(1)} + \nabla_0 \cdot \sum_\alpha w_\alpha f_\alpha^{(1)} \mathbf{e}_\alpha \mathbf{e}_\alpha\right) = -\frac{1}{\tau^*}\sum_\alpha w_\alpha \mathbf{e}_\alpha f_\alpha^{(2)}$$

Using Eqs. (2.15) and (2.18b), we obtain

$$\frac{\partial}{\partial t_1}(\rho \mathbf{u}) + \left(1 - \frac{1}{2\tau^*}\right)\nabla_0 \cdot \sum_\alpha w_\alpha f_\alpha^{(1)} \mathbf{e}_\alpha \mathbf{e}_\alpha = 0$$

Proceeding as before,

$$\sum_{\alpha} w_\alpha f_\alpha^{(1)} \mathbf{e}_\alpha \mathbf{e}_\alpha = \sum_{\alpha} (\mathbf{e}_\alpha - \mathbf{u})(\mathbf{e}_\alpha - \mathbf{u}) w_\alpha f_\alpha^{(1)} + \mathbf{uu} \sum_{\alpha} w_\alpha f_\alpha^{(1)} + 2\mathbf{u} \sum_{\alpha} w_\alpha \mathbf{e}_\alpha f_\alpha^{(1)} - 2\mathbf{uu} \sum_{\alpha} w_\alpha f_\alpha^{(1)}$$

Using Eq. (2.16) and the definition of pressure tensor, after some algebra, the momentum equation is retrieved in the following form:

$$\frac{\partial}{\partial t_1}(\rho \mathbf{u}) + \nabla_0 \cdot (\rho \mathbf{uu}) = -\nabla_0 \cdot \left[\left(1 - \frac{1}{2\tau^*} \right) \mathbf{P}^{(1)} \right] \tag{2.22}$$

Equations (2.20) and (2.22) denote the equations for conservation of momentum.

A careful choice of the discrete velocities, weight functions and the equilibrium distribution based on an appropriate lattice (D2Q9, for example) yields expressions for the pressure tensor in Eqs. (2.20) and (2.21) in a form that restores Euler equation and Navier-Stokes equation from Eq. (2.20) and Eq. (2.21) respectively. Using the values of $\mathbf{e}_\alpha$, w_α and $f_{eq,\alpha}$ for D2Q9 lattice mentioned before, the pressure tensors become

$$\mathbf{P}^{(0)} = c_s^2 \rho \mathbf{I} = p\mathbf{I} \tag{2.23a}$$

$$\mathbf{P}^{(1)} = -\tau^* \left[\left(\frac{1}{3} - \frac{c_s^2}{c^2} \right) (\nabla \cdot \mathbf{u}) \mathbf{I} + \frac{1}{3} \nabla \left\{ (\nabla \mathbf{u}) + (\nabla \mathbf{u})^T \right\} + \frac{\partial}{\partial t_0} (\rho \mathbf{uu}) \right] \tag{2.23b}$$

Some algebraic manipulation from Eq. (2.23) leads to the incompressible form of Navier-Stokes equation

$$\frac{\partial}{\partial t}(\rho \mathbf{u}) + \nabla \cdot (\rho \mathbf{uu}) = -\nabla p + \nu \nabla^2 \mathbf{u} \tag{2.24}$$

where $\nu = \left(\frac{2\tau^* - 1}{6} \right) c^2 \delta t$.

2.3.2 Numerical Implementation of Lattice Boltzmann Method

Equation (2.11) is usually solved in two steps as follows:

Collision Step: $$\tilde{f}_\alpha(\mathbf{r}_i, t+\delta t) = f_\alpha(\mathbf{r}_i, t) - \frac{1}{\tau^*}\left[f_\alpha(\mathbf{r}_i, t) - f_{eq,\alpha}(\mathbf{r}_i, t)\right] \tag{2.25a}$$

Streaming Step: $$f_\alpha(\mathbf{r}_i + \mathbf{e}_\alpha \delta t, t+\delta t) = \tilde{f}_\alpha(\mathbf{r}_i, t+\delta t) \tag{2.25b}$$

$\tilde{f}_\alpha$ represents a post-collision state. It needs to be emphasized that with such a splitting in the computational procedure, there is no need to store values of the distribution function at both time steps during the computation. Information on one time level is sufficient for unsteady flow simulations. [88]. The positivity of viscosity requires that $\tau^* > 0.5$. The pressure is obtained from the equation of state $p = \rho c_s^2$. The collision step is completely local. The streaming step involves no computation. Eq. (2.25) is explicit, easy to implement, and straightforward to parallelize.

As a computational tool, LBE method differs from NS equations based method in various aspects. The major differences are as follows [88]:

1. NS equations are second-order partial differential equations (PDEs); the DVM from which the LBE model is derived consists of a set of first-order PDEs. Such a difference in the nature of PDE's is also reflected in the discretized forms for each type of equations.
2. NS solvers inevitably need to treat the nonlinear convective term; the LBE method totally avoids the nonlinear convective term, because the convection becomes simple advection (uniform data shift).
3. CFD solvers for the incompressible NS equations need to solve the Poisson equation for the pressure. This involves global data communication, while in the LBE method data communication is always local and the pressure is obtained through an equation of state.

4. In the LBE method, the Courant-Friedrichs-Lewy (CFL) number is proportional to $\delta t = \delta x$; in other words, the grid CFL number is equal to 1 based on the lattice units of $\delta x = \delta t = 1$. Consequently, the time dependent LBE method is inefficient for solving steady-state problems, because its speed of convergence is dictated by acoustic propagation, which is very slow.
5. Boundary conditions involving complicated geometries require careful treatments in both NS and LBE solvers. In NS solvers, normal and shear stress components require appropriate handling of geometric estimates of normal and tangent, as well as one-sided extrapolation. In LBE solvers, the boundary condition issue arises because the continuum framework, such as the no-slip condition at the wall, does not have a counterpart.
6. Since the Boltzmann equation is kinetic-based, the physics associated with the molecular level interaction can be incorporated more easily in the LBE model. Hence, the LBE model can be fruitfully applied to micro-scale fluid flow problems.
7. The spatial discretization in the LBE method is dictated by the discretization of the particle velocity space. This coupling between discretized velocity space and configuration space leads to regular square grids. This is a limitation of the LBE method, especially for aerodynamic applications where both the far field boundary condition and the near wall boundary layer need to be carefully implemented.

The overall solution procedure for LBM can be described by the following algorithm, known as *stream and collide algorithm*:

1. Generate a square grid on the computational domain
2. Select a time step $\delta t = \delta x / c$
3. Initialize *f* values in all lattice directions at each grid point
4. At each grid point, calculate the macroscopic flow variables, ρ and **u** using Eq. (2.16).
5. *Collision Step*: Calculate 'ready to advect' distribution function at each grid point for each direction $\tilde{f}_\alpha(\mathbf{r},t) = f_\alpha(\mathbf{r},t) + \Omega_a(\mathbf{r},t)$ where $\Omega_a(\mathbf{r},t)$ is the collision term
6. *Streaming Step*: Advect the particle population in the direction of corresponding lattice velocity to the neighboring lattice node $f_\alpha(\mathbf{r} + \mathbf{e}_\alpha \delta t, t + \delta t) = \tilde{f}_\alpha(\mathbf{r},t)$

The requirement of square grids of uniform size is a major limitation of LBM. Although some recent works have used rectangular or stretched grids, most of the LBM works still use uniform square grids. One method adopted to overcome the requirement of fine grid resolution at specific locations in the computational domain is the use of multi-block methods. In this method, the computational domain is divided into several blocks and each block is divided into square lattices.

2.3.3 Boundary Conditions

As discussed in the previous section, imposition of boundary conditions is a non-trivial task in LBM. This is primarily because in LBM, one solves for the distribution function while the boundary conditions have to satisfy certain constraints of macroscopic variables. In particular, in traditional NS solvers, imposition of the correct velocity boundary conditions automatically ensures momentum conservation and no-slip

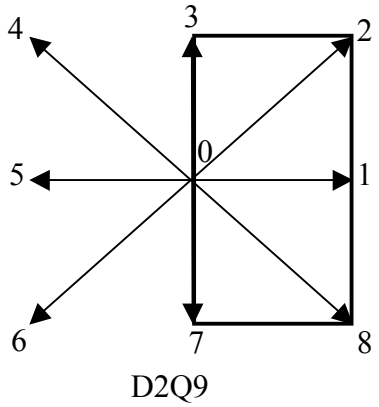

Figure 2.2. A typical boundary node.

conditions. On the other hand, for LBM, there is no analogue of no-slip condition and solutions that satisfy the constraint conditions do not necessarily conserve momentum flux.

The essence of the problem of imposition of boundary conditions in LBM can be understood from Fig. 2.2. In Fig. 2.2, a typical boundary node with its associated set of discrete lattice directions are shown. In the collision step, the 'ready to advect' distribution functions, $\tilde{f}$ are calculated for all the directions at each node including those on the boundary. However, during streaming step for the node shown in Fig. 2.2, distribution functions for directions 3, 4, 5, 6 and 7 can be advected from other nodes on the wall or in the interior. On the other hand, distribution functions in the directions 1, 2 and 8 have to be advected from locations outside the domain, for which no f value is available from streaming step. We need additional closure relations to estimate these values.

The simplest boundary condition in LBM is periodic boundary condition. In absence of any external influence other than periodic boundary conditions, the collision and streaming operations will eventually reduce all initial populations to uniform

equilibrium values irrespective of their initial values. To implement periodic boundary conditions in LBM, departing populations on outward pointing links are allowed to enter the domain through inward pointing links on the opposite boundary with no constraint on macroscopic velocity or density.

It is obvious that periodic boundaries cannot handle all flow configurations. For such situations, other boundary conditions like wall, velocity, pressure and outflow boundaries have to be incorporated. The most popular approach to model wall boundaries is the bounce-back method. In this approach, the momentum of the particle is bounced back in the opposite direction after it hits the wall. With reference to Fig. 2.2, a simple bounce-back scheme would close the boundary problems as

$$f_8 = f_4; \qquad f_2 = f_6; \qquad f_1 = f_5 \tag{2.26}$$

However, although the stream and collide algorithm is second-order accurate, the bounce-back algorithm, with the wall placed at a node (*bounce-back at node*) is only first order accurate. To overcome this difficulty, walls are placed at an intermediate position between nodes. When the wall is placed midway between nodes, the arrangement is often referred to as *bounce-back at link*. For such configurations, an additional layer of nodes is considered beyond the wall. The bounce-back condition is applied at the wall and transferred to the nodes by interpolation.

Zhou and He [96] developed LBM formulations for both velocity and pressure boundary conditions by extending the bounce-back concept to the non-equilibrium part of the distribution function. Referring to Fig. 2.2, first we consider a situation for which velocity is specified at the node. For this node, we can write

$$f_1 + f_2 + f_8 = \rho - f_0 - f_3 - f_4 - f_5 - f_6 - f_7 \tag{2.27}$$

$$f_1 + f_2 + f_8 = \rho u_x + f_4 + f_5 + f_6 \tag{2.28}$$

$$f_2 - f_8 = \rho u_y - f_3 - f_4 + f_6 + f_7 \tag{2.29}$$

From the condition of bounce-back of non-equilibrium component of nodes, $f_1 - f_1^{eq} = f_5 - f_5^{eq}$. Hence,

$$f_1 = f_5 - \left(f_5^{eq} - f_1^{eq}\right) = f_5 + \frac{2}{3}\rho u_x \tag{2.30}$$

From Eqs. (2.27) – (2.29),

$$f_2 = f_6 - \frac{1}{2}\left(f_3 - f_7\right) + \frac{1}{6}\rho u_x + \frac{1}{2}\rho u_y \tag{2.31}$$

$$f_8 = f_4 + \frac{1}{2}\left(f_3 - f_7\right) + \frac{1}{6}\rho u_x - \frac{1}{2}\rho u_y \tag{2.32}$$

Finally, density at that point is calculated from Eqs. (2.27) and (2.28) as

$$\rho = \frac{f_0 + f_3 + f_7 + 2\left(f_4 + f_5 + f_6\right)}{1 - u_x} \tag{2.33}$$

If pressure is prescribed at the boundary node instead of velocity, the procedure is similar for determination of the unknown distributions. However, in this case the velocities at the inlet are not known a priori. Instead, the pressure, and hence, the density (from the equation of state, $p = \rho c_s^2$) is known. Equation (2.33) is rearranged as

$$u_x = 1 - \frac{f_0 + f_3 + f_7 + 2\left(f_4 + f_5 + f_6\right)}{\rho} \tag{2.34}$$

Several other types of boundary conditions have been suggested in literature like consistent hydrodynamic boundary condition [97], extrapolation boundary condition [98], non-equilibrium extrapolation boundary condition [99], and specular bounce-back [100]. The last one is particularly suited for handling slip flows in microchannels.

CHAPTER 3

ELECTROOSMOTIC MIXING

3.1 Background

Specific manufacturing processes and coatings can be used to induce an electric potential on a surface when it comes in contact with an ionic liquid. This surface potential, called the *zeta* (ζ) *potential*, enables a neutral electrolyte solution to develop an electric double layer (EDL) very close to a surface. The value of the zeta potential depends on the surface material [101] and can be altered by use of specialized coatings [102]. The electric double layer thickness, which is the *Debye length*, depends on the molarity of the liquid, the valencies of the ions present, and the permittivity of the medium. Negatively charged liquid ions within this layer arrange themselves to lie closer to a positively charged surface and *vice versa*. The ions contained in the EDL move when an external electric field is applied, causing liquid motion within it. This induces motion throughout the domain through viscous shearing. Such electro-osmotic flows (EOFs) [103] have been used to enable mixing in various microscale applications such as for sample injection, chemical reactions and species separation [104,105].

Ng *et al*. [106] performed numerical simulations of EOF and mixing by considering a steady electric field and a nonuniform surface potential and were able to generate both in- and out-of-plane vortices, which could be combined to create streamwise vortices. Qian and Bau [107] provided closed form solutions for the flow and chaotic mixing in an electro-osmotic stirrer by considering a two-dimensional conduit

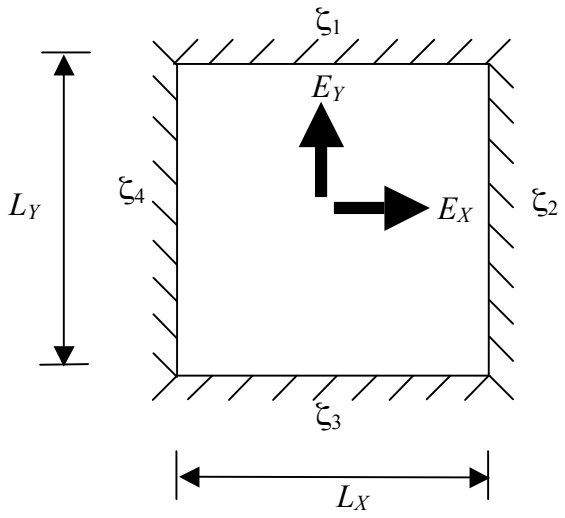

Figure 3.1. Schematic of electro-osmotic cavity.

with electrodes placed repeatedly in the flow direction. They found that an unsteady flowfield, which gave rise to chaotic mixing, could be established by altering the magnitude and sign of the ζ-potential provided by the individual electrodes. Stroock and McGraw [108] developed an analytical model by idealizing their configuration through a superposition of a pressure-driven axial flow and an electro-osmotic transverse flow for a staggered herringbone mixer. They demonstrated chaotic mixing that was produced by two transverse alternating flow patterns. Pacheco et al. [109] and Kim et al. [110] simulated mixing in channel flows by combining axially and transversely generated electrokinetic flows. The former investigation analyzed time-dependent flows, and the latter considered steady flows with a relatively complex potential distribution.

In contrast to these earlier studies, which relied on either unsteady flows or complex potential distributions, we present a relatively simpler scheme to achieve rapid mixing that uses a steady electric potential and a homogeneous zeta potential in an easily implemented configuration (Fig. 3.1). The previous investigations mostly considered

flow-through configurations such as channels and did not address electro-osmotic stirring in cavities whereas our work primarily addresses the latter configuration. For the low Reynolds number flows (Re « 1) encountered in microfluidics, the inertia term in the Navier-Stokes equation can be neglected so that the flowfield is obtained by solving the Stokes equation. A linearized model for three-dimensional microchannel flow can thus be based on the superposition of one-dimensional axial channel flow upon the two-dimensional transverse flow along any of its cross sections. The latter cross-sectional flow resembles that in a two-dimensional rectangular cavity. Our model can therefore also be used to simulate the electro-osmotic flow that is generated across the channel cross section, which can be superposed with the axial flow that is independent of it.

The simulation of electroosmotic flow requires exceedingly fine grids in the EDL to simulate the essential features of the flow and transport phenomena [111]. A popular alternative strategy [107,109,110] simplifies the treatment of the electro-osmotic flow by considering a Helmholtz-Smoluchowsky velocity, which is the fluid velocity at the edge of the EDL. Since the EDL thickness (~10–100 nm) is much smaller than the channel or cavity dimensions (~10–100 μm), this approach takes the condition at the EDL edge and applies it directly at the wall. This eliminates the need for the superfine spatial resolution required for analysing the EDL flow and thus considerably reduces the computational cost. Besides, the solution of electrostatic potential distribution is also not required. However, for smaller geometries, dilute solutions or relatively large EDL dimensions, the approximation is often questionable.

We have simulated the electro-osmotic flow using the lattice Boltzmann method (LBM), which is linear and based on a fully explicit scheme, and is easily implemented

on parallel computers [112] (Ladd 1997). These features of LBM make it an attractive method for analyzing electrokinetic flows with sufficient spatial resolution in the EDL. The method has been used to investigate microfluidic [86,113] and isothermal electrokinetic problems [114,115]. We have quantified the mixing generated through the mixing efficiency.

3.2 Mathematical Modeling

3.2.1 Electroosmotic Mixing

The governing relations for electroosmotic flow represent a coupled fluid-electrostatic phenomenon. The fluid motion is governed by the continuity and Navier-Stokes equations (which include the electro-osmotic body force), i.e.,

$$\nabla.\mathbf{u} = 0 \text{, and } \rho\frac{\partial \mathbf{u}}{\partial t} + \rho\mathbf{u}\cdot\nabla\mathbf{u} = -\nabla p + \mu\nabla^2\mathbf{u} + \rho_e\mathbf{E}_{eff} \text{,} \qquad (3.1a, b)$$

where $\mathbf{E}_{eff}$ denotes the effective electric field (both applied electric field and that due to the wall zeta potential). For a static or quasi-static irrotational electric field, it is related to electric potential Φ in the form $\mathbf{E}_{eff} = -\nabla\Phi$. The electric potential results in a spatial charge distribution following the Poisson equation

$$\nabla^2\Phi = -\frac{\rho_e}{\varepsilon} \text{,} \qquad (3.2)$$

where $\rho_e = \sum_i z_i e n_i$ denotes the volumetric free charge density (n_i denotes the number concentration of ions of species i) and ε is the permittivity of the medium. The electric charge distribution depends both on the potential due to the applied electric field ϕ and the wall zeta potential ψ (*i.e.*, $\Phi = \phi + \psi$). When, (i) the Debye thickness is small compared with the channel diameter or height (in our case the ratio of Debye length to

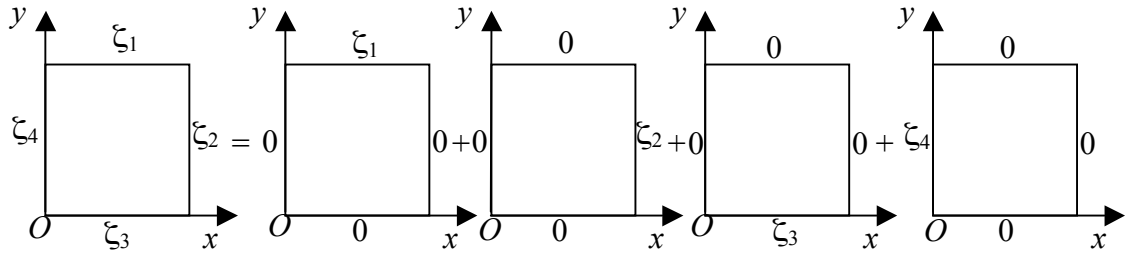

Figure 3.2. One problem with four non-zero boundary conditions is divided into four problems with each having one non-zero boundary condition. The solution of the original problem is the sum of the solution of the four problems.

channel dimension is 0.01) and (ii) the charge at the walls is not large (i.e., $ze\psi/k_BT \leq 1$), then $\nabla\phi << \nabla\psi$. At the same time, if the fluid velocity in the microchannel is very small (generally for microchannel flows, Re « 1), Eq. (3.2) assumes the forms [116,117]

$$\nabla^2\phi = 0 \text{, and } \nabla^2\psi = -\frac{\rho_e}{\varepsilon} \text{,} \tag{3.3a, b}$$

For flows over a non-conducting stationary surface, the ion distribution can be approximated by the Boltzmann distribution $n_i = n_{i\infty}\exp(-z_i e\psi/k_BT)$. For the symmetric electrolyte ($z_i = \pm z$, $n_i = n_\infty$) considered in this study, the charge density

$$\rho_e = n_\infty ze\left(\exp\left(-\frac{ze\psi}{k_BT}\right) - \exp\left(\frac{ze\psi}{k_BT}\right)\right) = -2n_\infty ze Sinh\left(\frac{ze\psi}{k_BT}\right) \tag{3.4}$$

Substituting Eq. (3.4) into Eq. (3.3b) leads to Poisson-Boltzmann equation,

$$\nabla^2\psi = \frac{2n_\infty ze}{\varepsilon} Sinh\left(\frac{ze\psi}{k_BT}\right). \tag{3.5}$$

For a small value of the zeta potential ($ze\psi/k_BT \leq 1$), Eq (3.5) can be approximated using the Debye-Hückel approximation,

$$\nabla^2\psi = \frac{2n_\infty z^2 e^2 \psi}{\varepsilon k_B T} = \kappa^2 \psi \quad , \tag{3.6}$$

where κ^{-1} denotes the Debye length. This approach has been adopted to simulate electroosmotic flows in cavities [111] and rectangular channels [110] when a transverse potential gradient is applied. Equation (3.6) can be analytically solved by separating variables [118] to determine the electric potential and charge distribution.

The boundary conditions (c.f. Fig. 3.2) are

$$\psi(0,y) = \zeta_4; \qquad \psi(L_x,y) = \zeta_2; \qquad \psi(x,0) = \zeta_3; \qquad \psi(x,L_y) = \zeta_1. \tag{3.7}$$

This single problem containing four non-zero boundary conditions can be divided into four simpler problems, each with a single non-zero boundary condition as shown in Fig. 3.2 [118]. If ψ_j is the solution of the jth problem (j = 1, 2, 3, 4) then the solution of Eq. (3.6) with boundary condition (3.7) is

$$\psi(x,y) = \sum_{j=1}^{4} \psi_j(x,y) \quad . \tag{3.8}$$

Considering one of these four new problems (namely, j = 1) in the context of Eq. (3.6), the relevant boundary conditions are

$$\psi_1(0,y) = 0; \qquad \psi_1(L_x,y) = \zeta_2; \qquad \psi_1(x,0) = 0; \qquad \psi_1(x,L_y) = 0 \quad . \tag{3.9}$$

We separate variables by substituting $\psi_1(x,y) = X(x)Y(y)$ in Eq. (3.6) to obtain

$$\frac{Y''}{Y} = \kappa^2 - \frac{X''}{X} = -\gamma^2 \quad , \tag{3.10}$$

where γ is a real constant. The negative sign before γ^2 ensures a Sturm-Liouville system in the y-direction. The general solution to Eq. (3.10), therefore, becomes

$$\psi_1(x,y)=\sum_{n=1}^{\infty} A_n \sin(\gamma_n y)\sinh(\eta_n x) \quad , \tag{3.11}$$

where $\eta_n = \sqrt{\gamma_n^2 + \kappa^2}$ and $\gamma_n = n\pi/L_y$, for $n = 1, 2, \ldots$.

The constants A_n are obtained using the remaining boundary condition upon Fourier expansion, i.e.,

$$A_n = \frac{2\zeta_2\left(1-\cos(n\pi)\right)}{\gamma_n L_y \sinh(\eta_n L_x)} = \frac{2\zeta_2\left(1-(-1)^n\right)}{n\pi \sinh(\eta_n L_x)} \quad . \tag{3.12}$$

Therefore, the solution for this problem is

$$\psi_1(x,y) = \sum_{j=1}^{4} \frac{2\zeta_2\left(1-(-1)^n\right)}{n\pi \sinh(\eta_n L_x)} \sin(\gamma_n y)\sinh(\eta_n x) \quad . \tag{3.13}$$

Likewise, we can solve the other three problems. Following Eq. (3.8) the solution of the original problem (Eq. (3.6) with boundary condition (3.7)) is

$$\begin{aligned}\psi(x,y) = &\sum_{n=1}^{\infty} \zeta_1 \frac{2\left(1-(-1)^n\right)}{n\pi \sinh\left(\mu_n L_y\right)} \sin(\lambda_n x)\sinh(\mu_n y) + \sum_{n=1}^{\infty} \zeta_2 \frac{2\left(1-(-1)^n\right)}{n\pi \sinh(\eta_n L_x)} \sinh(\gamma_n x)\sin(\eta_n y) \\ &+ \sum_{n=1}^{\infty} \zeta_3 \frac{2\left(1-(-1)^n\right)}{n\pi \sinh\left(\mu_n L_y\right)} \sin(\lambda_n x)\sinh\left(\mu_n\left(L_y - y\right)\right) + \sum_{n=1}^{\infty} \zeta_4 \frac{2\left(1-(-1)^n\right)}{n\pi \sinh(\eta_n L_x)} \sinh\left(\gamma_n\left(L_x - x\right)\right)\sin(\eta_n y)\end{aligned} \quad , \tag{3.14}$$

where $\lambda_n = \frac{n\pi}{L_x}$, $\mu_n = \sqrt{\lambda_n^2 + \kappa^2}$, $\gamma_n = \frac{n\pi}{L_y}$, $\eta_n = \sqrt{\gamma_n^2 + \kappa^2}$.

Equations (3.1 a, b) are solved to generate the flowfield using LBM. The body force per unit mass responsible for the EOF is

$$\mathbf{a} = \frac{\rho_e}{\rho}\left(\mathbf{E} - \nabla\psi\right) = -\frac{\kappa^2 \varepsilon \psi}{\rho}\left(\mathbf{E} - \nabla\psi\right) = -\frac{\kappa^2 \varepsilon}{\rho}\left(\psi\mathbf{E} - \frac{1}{2}\nabla\psi^2\right) \quad . \tag{3.15}$$

where $\mathbf{E} = -\nabla\phi$ denotes the external electric field. The first term in parentheses is responsible for fluid flow along the wall and is used to calculate **a**. The second term

$\frac{1}{2}\nabla\psi^2$ is normally neglected in the literature on electro-osmotic flow in comparison with the first tem in the parenthesis, $\psi\mathbf{E}$. Our contribution is through the inclusion of this term which extends the formulation to cases involving large gradients in streaming potential. This term, can be added to ∇p to obtain an effective pressure gradient $\nabla p' = \nabla(p + \frac{1}{2}\psi^2)$, which increases the pressure near the wall. A similar inclusion of gradients of scalar potentials has been reported in the context of buoyancy-driven flows [119,120] and thermomagnetic convection [121] in enclosures. The pressure can be obtained form the relation $p' = \frac{1}{3}\rho c^2$. At all the four walls no-slip boundary condition is applied as proposed by Zou and He [96] as discussed in Chapter 2.

We consider electroosmotic mixing in a 10μm×10μm cross-section square enclosure where the four walls can have different but homogenous ζ potentials (Fig. 3.1). We assume that the Debye length ≈100nm, which can be generated in an aqueous monovalent ion solution of 10^{-6} M concentration. The electric potential ψ is normalized by the term k_BT/ze (= 25.69 mV for z = 1). The normalized electric field $E^* = E/(k_BT/ze\delta x)$. For a square cavity of 10 μm sides with 501 node points (δx = 20 nm), E^* = 1 is equivalent to a dimensional value of 1.28 V/μm. The fluid properties such as density, viscosity, and permittivity are assumed to be those of water.

3.3 Results and Discussions

3.3.1 Validation

We validate our LBM simulations against a benchmark solution for a lid driven cavity flow [122]. Results are presented in Fig. 3.3 for three different Reynolds numbers

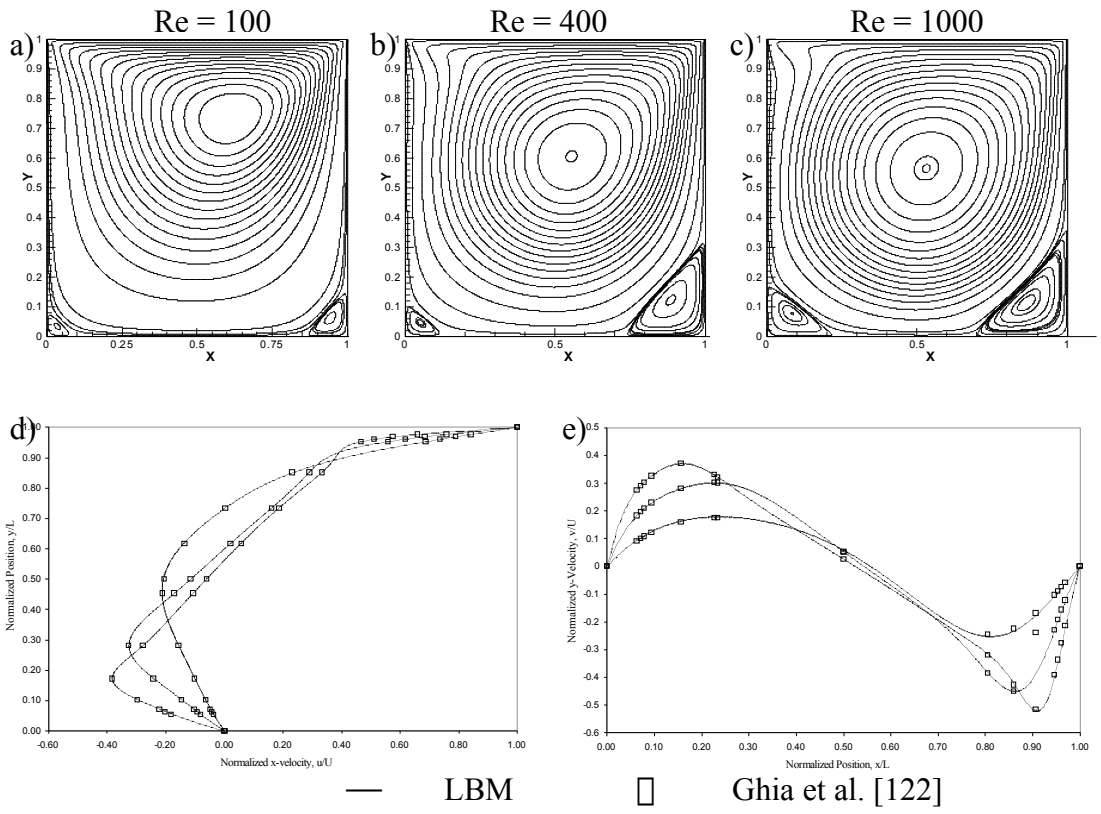

Figure 3.3: Validation of LBM code against benchmark solution of lid-driven cavity flow problem by Ghia et al. [122]

a)-c) Streamline patterns for different Reynolds numbers.

d) x-velocity for mid vertical plane.

e) y-velocity for mid horizontal plane.

(100, 400 and 1000) defined with respect to the top wall velocity and the cavity width. Figures 3.3(a)-(c) present the streamlines generated when the top lid of the cavity is driven towards the right. The center of the primary vortex moves toward the cavity center with increasing Reynolds number and the secondary vortices generated at the bottom left and right corners grow in size in accord with the results in Ref. 122. The x-wise velocity along the mid-vertical plane and y-component along the mid-horizontal plane are presented in Figs. 3.3(d) and (e). The squares denote results from Ref. 122 while lines

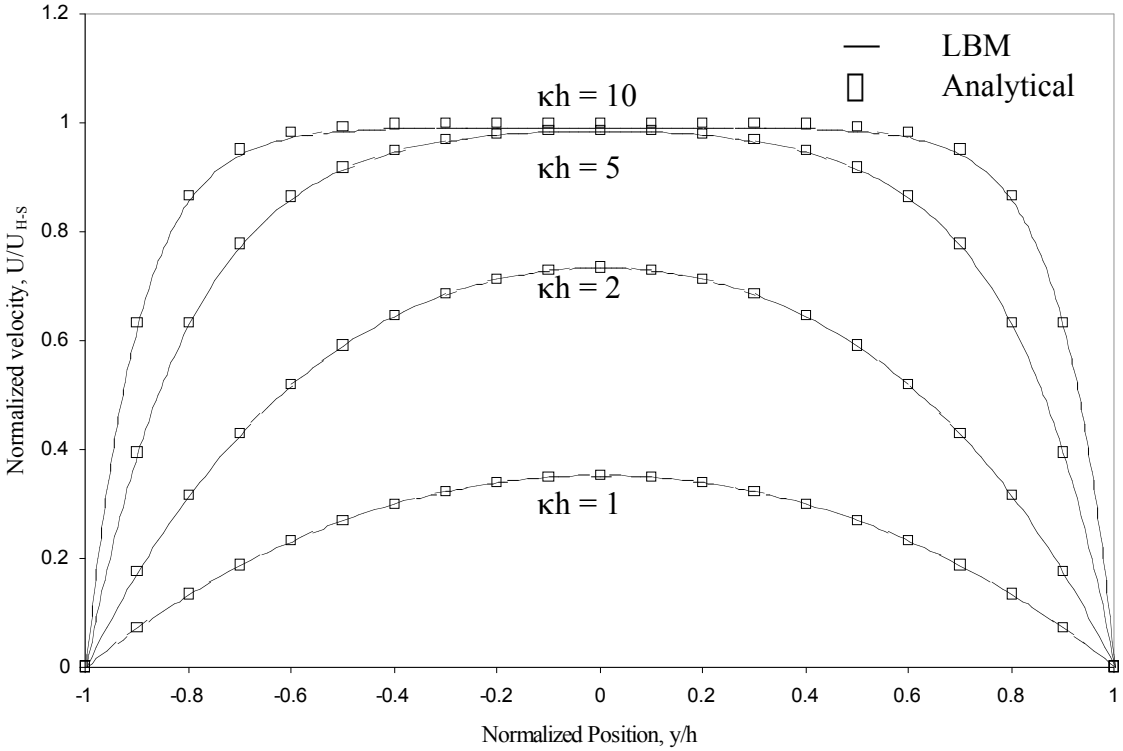

Figure 3.4: Comparison between fully developed electro-osmotic velocity profile obtained by using LBM and that obtained analytically.

represent results from the LBM simulations. Our results are in full agreement with the benchmark solutions. The minimum stream function values and locations for the primary vortices, provided in Table 3.1, compare equally favorably. The maximum difference, which occurs due to rounding off, is less than 0.8%.

Table 3.1: Comparison of the minimum value of stream function of the primary vortex and its location for different Reynolds number.

	Re = 100			Re = 400			Re = 1000		
	Ψ_{min}	X	Y	Ψ_{min}	X	Y	Ψ_{min}	X	Y
Ghia et al.	-0.1034	0.617	0.734	-0.1139	0.555	0.606	-0.1179	0.531	0.563
LBM	-0.1028	0.618	0.736	-0.1129	0.556	0.604	-0.1170	0.532	0.562

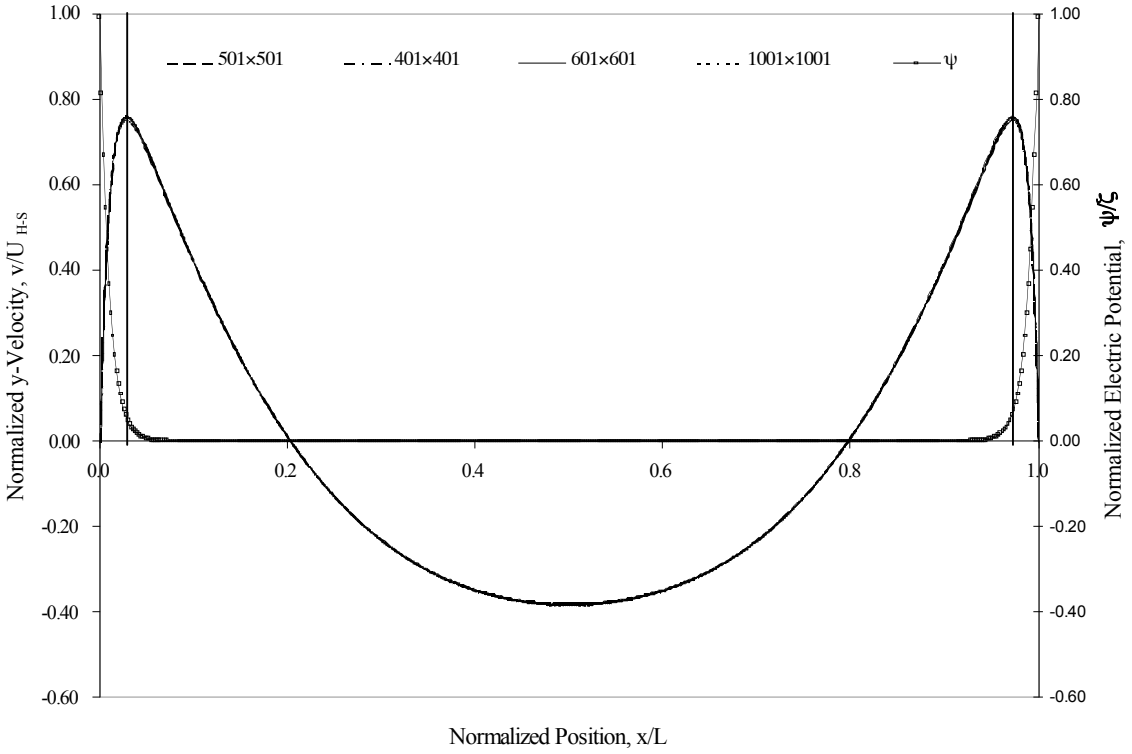

Figure 3.5: Comparison of y-velocity profile at the mid horizontal plane for case II obtained by using different grid resolutions and the distribution of electric potential along the plane.

We have also validated our simulated model against the corresponding analytical solution by simulating fully developed EOF in channel for different κh values, where h denotes the half channel width. The analytical solution for the velocity [103] is

$$U/U_{H\text{-}S} = 1 - \cosh(\kappa h\, y/h)/\cosh(\kappa h). \quad (3.16)$$

Fig. 3.4 presents a comparison between the analytical results (squares) and the LBM simulations (lines). Both sets are again in excellent agreement.

3.3.2 Grid Independence

The grid independence of the LBM simulations is examined in context of Case II in Table 3.2**.** Here, the left and right walls were provided with unit zeta potential and an upward electric field $E^*_Y = 0.01$ is applied. The simulation is run for four different grid resolutions, namely, 401×401, 501×501, 601×601 and 1001×1001. The velocity along the y-direction, normalized with the Helmohltz-Smoluchowski velocity $U_{H\text{-}S}$, is plotted for all four cases at the mid-horizontal plane in Fig. 3.5. The figure also presents the potential distribution inside the cavity. The velocity profiles are virtually identical for all grid resolutions with imperceptible differences close to the walls. The maximum velocity is found to be approximately 75% of H-S velocity at the edge of EDL where electric potential decreases to zero. A grid size of 501×501 is selected since it provides a virtually identical solution to the finer 1001×1001 grid.

3.3.3 Mixing

We consider fluid mixing due to different homogeneous wall zeta potentials in the presence of a steady applied electric field for which the various cases are listed in Table 3.2. At first, the flowfield is obtained by solving the lattice Boltzmann equation as discussed in the previous section. Once the steady flow field is obtained a number of passive tracer particles are introduced in the flow. The motion of a tracer particle is obtained by solving the relation $\frac{d\mathbf{R}}{dt} = \mathbf{u}$, where $\mathbf{R} = (x, y)$ denotes the particle position and $\mathbf{u}$ the fluid velocity at that location. The above equation is solved using an explicit Euler Method and selecting the time step δt such that $\mathbf{u}\delta t \approx 0.01\boldsymbol{\delta}\mathbf{r}$, where $\boldsymbol{\delta}\mathbf{r}$ denotes the lattice spacing. Two types of passive tracer particles, white and black, are introduced into

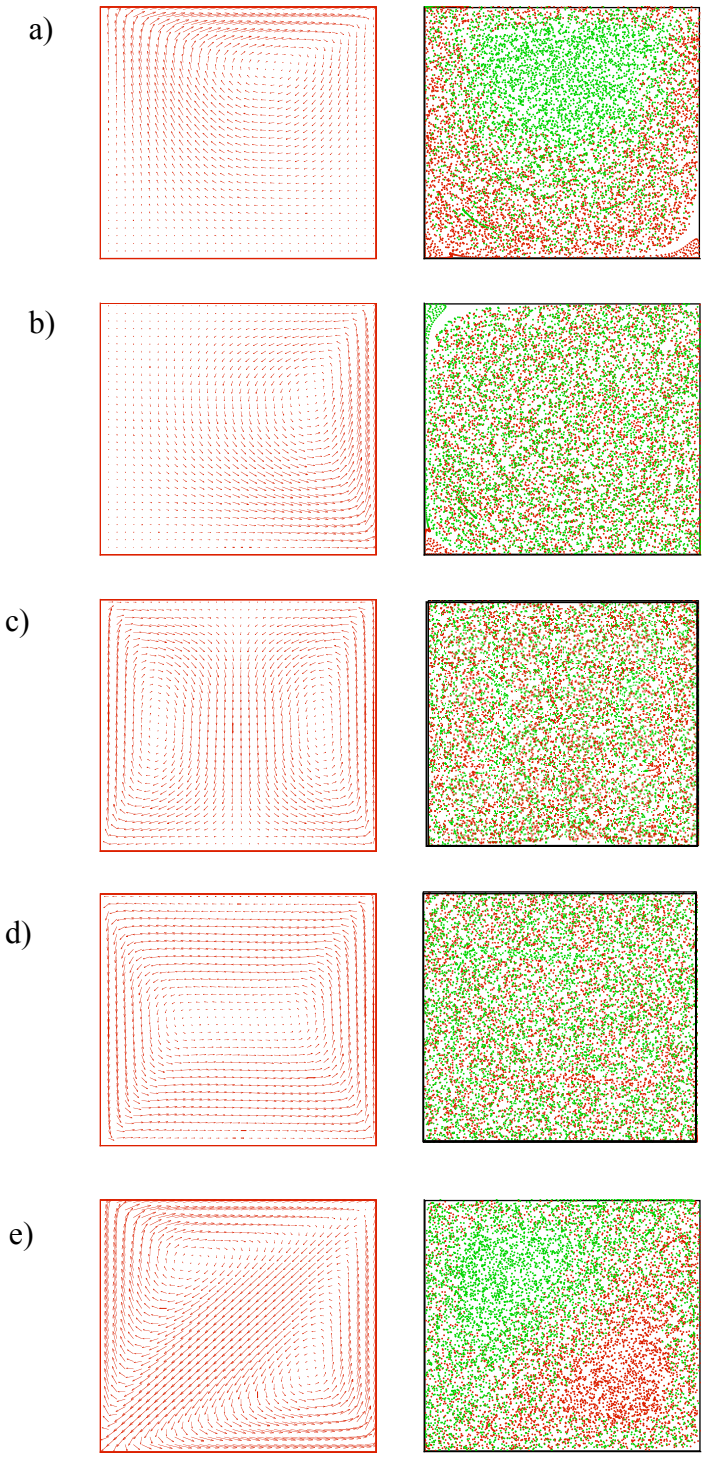

Figure 3.6. Steady state velocity vector and passive tracer particle locations for different cases listed in Table 3.2.

the top and bottom halves of the cavity, respectively. The resulting visualization of mixing by observing the motions of the passive tracers is purely that due to advection.

Table3.2: The different configurations related to electroosmotic mixing investigated.

Case No.	Non-Dimensional Zeta Potential				Non-Dimensional Electric Field	
	ζ_1	ζ_2	ζ_3	ζ_4	E^*_X	E^*_Y
I	1.0	0.0	0.0	0.0	0.01	0.0
II	0.0	1.0	0.0	0.0	0.0	0.01
III	0.0	1.0	0.0	1.0	0.0	0.01
IV	0.0	1.0	0.0	-1.0	0.0	0.01
V	1.0	1.0	1.0	1.0	0.01	0.01

Fig. 3.6 presents the steady state velocities and equilibrium tracer particle distributions for Cases I-V. Fig. 3.6(a) presents results for Case I, when $\zeta = 1$ for the top horizontal wall while $\zeta = 0$ for all other walls, and an electric field $E^*_X = 0.01$ is applied in the x-direction. This produces an EDL very close to the top surface, and the electric field forces the fluid to circulate clockwise inside the cavity. The center of the vortex is very close to the top surface and the circulation loops lie primarily within the top half of the cavity. Consequently, the tracer particles in the upper and lower halves of the cavity remain confined in those portions, although a few, close to the vertical wall, move between these halves. The white particles are mostly concentrated in the top half following the fluid circulation while a few others become sparsely distributed elsewhere.

Fig. 3.6(b) corresponds to Case II when $\zeta = 1$ for the right wall with the other walls at $\zeta = 0$. An EDL is again produced close to the right wall. With $E^*_Y = 0.01$ applied in the upward direction, the fluid near the right wall also moves upwards inducing circulation and good mixing in the right half of the cavity

Fig. 3.6(c) presents similar results for Case III when the two vertical walls are imparted unit zeta potentials while the horizontal walls are maintained at $\zeta = 0$, and an

upward field $E_Y^* = 0.01$ is applied. Two EDLs are formed along the two vertical walls for this case, which induce upward fluid motion along both interfaces. This results in two symmetric circulations within the cavity, one clockwise and the other counter-clockwise. The tracer particles are thus able to move and mix vertically, except at the center of their respective vortices, but those that originate within the right or left halves remain confined to those sections.

The mixing for Case IV is presented in Fig. 3.6(d) for which the right and the left walls are given unit positive and negative zeta potentials, respectively, while the applied electric field acts upward. The fluid along the right wall starts moving upward while that along the left moves down, creating circulation in the entire cavity. At the end, particles of both kinds are well mixed throughout the domain.

Results for case V are shown in Fig. 3.6(e) when all walls have unit positive zeta potentials while the applied field is along both the x and y directions ($E_X^* = 0.01$, $E_Y^* = 0.01$). This zeta potential distribution results in the formation of four EDLs, one along each wall. The fluid along the two vertical walls moves upward as a result while that along the horizontal walls moves rightward, which results in two triangular circulations inside the cavity. The tracer particles at the centers of vortices remain in the corners while other particles move diagonally creating two relatively unmixed triangular regions.

Mixing can be characterized through the mixing efficiency [123] or the Shannon entropy [124], which are interrelated. To do so, we divide the entire domain into a number of cells, and determine the number of green and red particles present in each of them. The $i \times j$ cells (i representing rows and j columns) in the domain are initially filled

with N_1 and N_2 numbers of green and red particles respectively. Since the two mixing quantities provide equivalent descriptions, we present results for the mixing efficiency only.

Mixing efficiency

The uniformity of mixing is measured by the mixing efficiency, which represents the standard deviation of mixing. If the k^{th} cell has n_1^k and n_2^k particles, respectively, of the two types, the mixing efficiency [123]

$$\sigma = \sqrt{\sum_{k=1}^{i\times j} \omega^k \left[\frac{n_1^k}{n_1^k + n_2^k} - \frac{N_1^k}{N_1^k + N_2^k} \right]^2}, \tag{3.17}$$

where, $\omega^k = (n_1^k + n_2^k)/(N_1 + N_2)$ denotes the weighting factor. For binary mixing with the material ratio 1:1 (i.e., $N_1 = N_2 = N$), the standard deviation σ ranges from 0 for complete mixing to 0.5 for nonmixed particles.

Shannon Entropy

Another parameter used to quantify mixing is the Shannon Entropy [124],

$$S = -\sum_{j=1}^{N_C} P_j \sum_{i=1}^{N_S} P_{i/j} \ln\left(P_{i/j}\right), \tag{3.18}$$

where P_j denotes the probability of finding a particle in j^{th} cell and $P_{i/j}$ the probability of finding an i^{th} species particle in the j^{th} cell. Mathematically, $P_j = (n_1^j + n_2^j)/(N_1 + N_2)$ and $P_{i/j} = n_i^j/(N_1 + N_2)$. Initially, the particles are introduced in an organized manner resulting in very low entropy. The entropy increases as the particles mix and are randomly distributed, reaching a maximum value S_E if the two species become perfectly mixed.

For perfect mixing, all cells have an equal number of particles of both species, i.e., $n_1^j = n_2^j = n^j$. This implies that $P_{1/j} = P_{2/j} = 0.5$. For $N_1 = N_2 = N = \sum n^j$, $P_j = 2n^j/2N = n^j/N$. Using these values in Eq. (3.17),

$$S_E = -\frac{\ln(0.5)}{N}\sum_{j=1}^{N_C} n^j = \ln 2 \quad , \tag{3.19}$$

where N_C denotes the total number of cells. The corresponding Shannon entropy mixing index, $I = S/S_E$ [125] varies between zero for an entirely unmixed state and 1 for fully mixed.

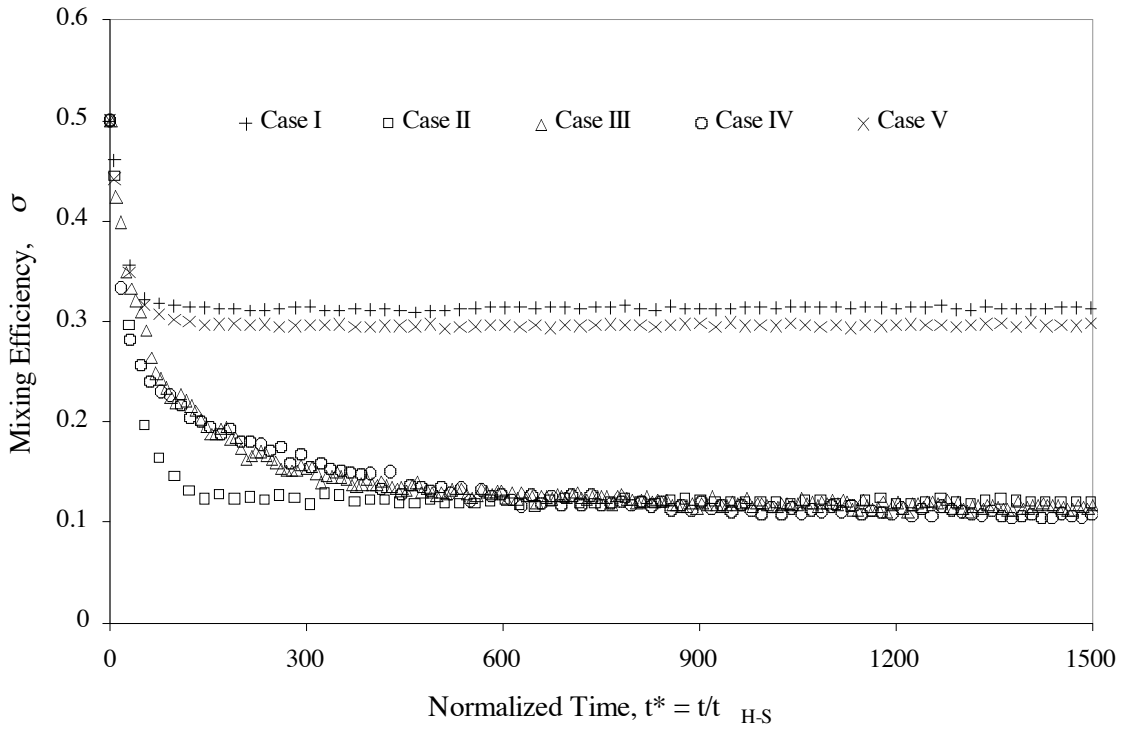

Figure 3.7. Variation in the mixing efficiency with respect to the normalized time for the different cases listed in Table 3.2.

Percentage of mixing

The percentage of mixing r varies between 0 and 100, which are limits for completely unmixed and fully mixed conditions. In general, for an arbitrary condition, r% of the domain could have two fluids completely mixed, for which $\sigma = 0$ and I = 1 while the remaining portion (100–r)% will have the values $\sigma = 0.5$ and I = 0. The mixing efficiency of the entire domain $\sigma^2 = 0.5^2 \times (1 - r/100)$ i.e., $r = 100\left(1 - \frac{\sigma^2}{0.25}\right)$. Consequently, I = r/100, indicating that the index also measures the percentage of mixing. Combining these two relations, $\mathbf{I} = \left(1 - \frac{\sigma^2}{0.25}\right)$.

The accuracy of these mixing parameters depends on the numbers of tracer particles and cells used in their determination. Considering a large number of cells increases the resolution but also increases the probability of finding spurious local nonhomogeneities, e.g., when only a single particle is present in a cell. It is therefore important to optimize the number of cells and particles used. We found that 10^4 particles and 20×20 cells provided useful measures of the mixing parameters for our simulations.

As mixing efficiency and Shannon entropy index are interrelated, we have plotted only mixing efficiency to study mixing.

The temporal evolution of the mixing parameter is normalized by the time scale, $t_{H\text{-}S} = L/U_{H\text{-}S}$ where $\mathbf{U}_{H\text{-}S} = \mu_{EO}\mathbf{E}$ is the Helmholtz-Smoluchowski electro-osmotic velocity, Here, **E** denotes the applied electric field and μ_{EO} the electro-osmotic mobility of the ions. The ion mobility depends on the wall ζ potential, the permittivity of the medium, and the fluid viscosity through the relation $\mu_{EO} = \varepsilon\zeta/\mu$.

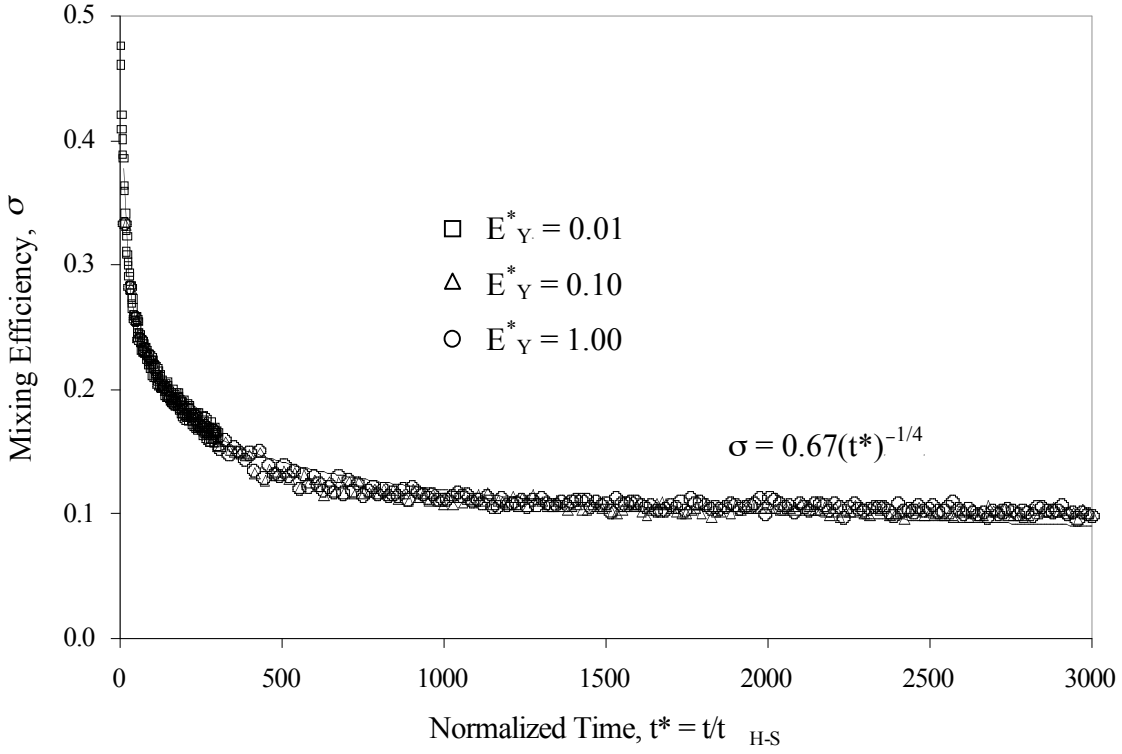

Figure 3.8. Variation of mixing efficiency with normalized time $t^*=t/t_{H\text{-}S}$ for different electric field strengths.

The tracer particles are initially entirely unmixed, i.e., $\sigma = 0.5$. The evolution of mixing efficiency is presented in Fig. 3.7. With the progression of mixing, the value of σ decreases. The mixing efficiency is overall poor for Cases I and V, reaching the minimum values $\sigma_{min}\approx 0.33$. This result concurs with Fig. 3.6, which shows that for Case I most particles remain in their respective halves of the cavity, and form two discrete triangular regions for Case V. Mixing improves for Cases II, III and IV. Case II produces the most rapid mixing ($\sigma_{min} \approx 0.12$), while Cases III and IV produce slower but marginally better mixing ($\sigma_{min} \approx 0.11$).

Next, we investigate the influence of varying E_Y^* between 0.01 and 1 for Case III. Fig. 3.8 presents the corresponding changes in σ. The plots for the variation of σ over t^* collapse on each other, yielding the relation $\sigma = 0.67t^{*-¼}$. This implies that the quality of mixing (i.e., the minimum value of σ) can be described by considering the normalized time alone. When the value of **E** increases but t^* is held constant, the dimensional time t required to achieve a specific σ value decreases, i.e., mixing occurs more rapidly. Decreasing the mixing time involves decreasing the channel length thus aiding miniaturization. According to Fig. 3.8, the equilibrium value of σ is reached at $t^* \approx 1000$. The actual mixing time can be calculated by using the relation $t^* = t/t_{H\text{-}S}$, as previously discussed. A time $t^* = 1000$ corresponds to $t \approx 73$ s for $E_Y^* = 0.01$, while for $E_Y^* = 0.1$ and 1.0, the value of $t \approx 7.3$ s and 0.73 s, respectively. On the other hand, the diffusion time scale $t_D = L^2/D \approx. 10^3–10^4$ s for L = 10 μm and diffusivity D of water-soluble organic molecules $\approx 10^{-14}–10^{-13}$ m^2/s [126].

Similar effects of electric field strength (E_X^* and E_Y^*) on σ were observed for all other configurations in Table 3.2. Consequently, similar to the analysis of case III, it is possible to generate different power series correlations between σ and t^* for other configurations.

CHAPTER 4

MAGNETIC ASSISTED MIXING

4.1 Background

Since the appearance of the concept of μ-TAS, suspensions of magnetic particles are being used in microfluidics for chemical or biomedical applications [127,128]. Both magnetic microparticles and ferrofluids have been studied to enhance mixing. In presence of an externally applied magnetic field, the magnetic microparticles acquires magnetic dipole moment, which interact with each other to form chain like structures, which can work as a stirrer [129,130]. These chains are rotated with the help of a rotating magnetic field to stir the fluids and enhance mixing [131]. Although magnetic microstirrers enable efficient mixing, they typically involve moving parts and are difficult to package and seal [64,132]. On the other hand, ferrofluid forms an agglomeration and can be easily maneuvered with the help of a suitable magnetic field. Such ferrofluid agglomeration is used as a piston to generate oscillatory motion in the fluids, thereby performing a "shaking" action [133]. Magneto-hydro-dynamics (MHD) micromixers [134] utilize Lorentz force to agitate fluids and induce secondary complex chaotic flows. However, Lorentz force is proportional to the fluid volume and as the microchannel dimensions are scaled down to smaller values, the agitation force is too small to induce sufficient chaos. In addition, MHD mixers can only be used for conductive fluids.

Recently magnetic particle actuation has received great interest because of its potential application in the field of microbiological assay system [128,135]. It is widely

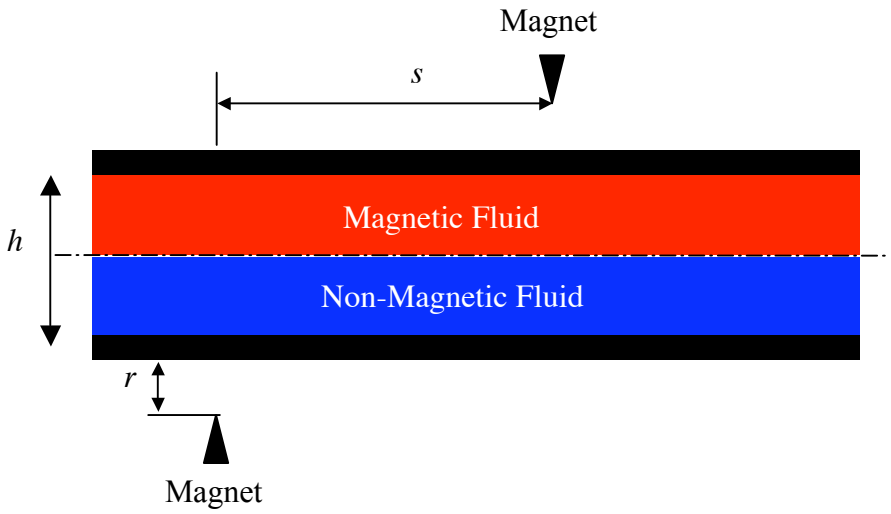

Figure 4.1. Schematic of the configuration.

used for detecting bateria in contaminated water, where the antibody coated magnetic particles are used to attach bacteria on it [136]. The magnetic particles with the bacteria attached to them are collected afterwards by using suitable magnetic field and treated with certain buffer solutions to generate optical signals characteristic to the presence of bacteria. Actuated by magnetic forces, the suspended magnetic particles can add agitation and chaotic advection in the fluid flows and thus enhances the mixing [129,137,138].

We consider a different magnetic method, i.e., ferrohydrodynamics involving ferrofluid transport, to induce mixing between two fluids. Ferrofluids are electrically nonconducting magnetic fluids that contain 5-15 nm diameter single domain superparamagnetic nanoparticles, usually of iron oxides. Since these particles are coated with an adsorbed surfactant layer to prevent agglomeration due to Van der Waals forces, they are able to form a stable colloid so that a ferrofluid can be considered as a single homogeneous liquid [139,140]. The bulk motion of a ferrofluid can be altered by applying an external magnetic field, the effects of which are more effective as the length

scale is reduced [141,121]. We simulate the mixing of a ferrofluid with a nonmagnetic fluid using a two-dimensional lattice Boltzmann method (LBM) [86 – 89], which has been previously employed to investigate microfluidic problems [87,113].

4.2 Objective

The objective of this study is to simulate the 2-D channel flow using the lattice Boltzmann method (LBM). In our simulations, two fluids are introduced through a microchannel of height h (taken as 50 μm in the simulations), as shown in the schematic of Fig. 4.1. Initially, the top half of the microchannel contains a dilute ferrofluid (with a 3% by volume concentration of magnetic nanoparticles), while a nonmagnetic fluid flows through its bottom half. A pair of magnets, both modeled as line dipoles of strength m, are placed alternately across the microchannel at a distance s apart from each other and at a displacement r from the exteriors of the microchannel walls. The magnet closest to the microchannel entrance is placed below the bottom microchannel wall while the other is positioned above the top wall. The magnetic field thus created causes the ferrofluid to crisscross the microchannel, which generates vortical motion and enhances mixing. By doing so, the magnetic nanoparticles contained in the ferrofluid also mix with the nonmagnetic fluid, which can be desirable for immunomagnetic assays and other chemical applications.

4.3 Mathematical Modeling

4.3.1 Multicomponent Lattice Boltzmann Method

The fundamental concept defining the lattice Boltzmann method (LBM) [142] is the construction of simplified kinetic models that incorporate the essential physics of microscopic and mesoscopic processes so that the averaged macroscopic properties obey the desired macroscopic equations [86]. The Boltzmann equation for single component with the Bhatnagar-Gross-Krook (BGK) approximation is [113]

$$\left(\frac{\partial}{\partial t} + \mathbf{e}\cdot\nabla_{\mathbf{r}} + \mathbf{a}\cdot\nabla_{\mathbf{e}}\right) f(\mathbf{r},\mathbf{e},t) = Q \quad , \tag{4.1}$$

where $f(\mathbf{r}, \mathbf{e}, t)$ is a one-particle probability distribution function, defined such that, $[f(\mathbf{r}, \mathbf{e}, t).d^3\boldsymbol{r}.d^3\boldsymbol{e}]$ is the number of particles which, at time t, are located within a phase-space control element $[d^3\boldsymbol{r}.d^3\boldsymbol{e}]$ about **r** and **e** (**r** is the particle's co-ordinate in physical space and **e** is the particle's discrete velocity) [89]. Here, **a** is the external force per unit mass acting on the particle. The last term, Q of the above equation represents the collision between the two particles.

There are a number of multicomponent lattice Boltzmann models [143,144,145]. Models can be based on free energy theory, but not yield a correct hydrodynamic equation [144,145]. Others are based on the single fluid theory for which an *ad hoc* equilibrium velocity is used in the equilibrium distribution of f to satisfy the conservation laws [143]. Consequently, the viscous and diffusion relaxation processes are dependent. These models cannot be applied for mixtures of species with significantly different properties. Thus, we use a more plausible model that is derived from the continuous kinetic equations [146].

Following the similar procedure for a single species lattice Boltzmann equation, we can derive N simultaneous equations for N-species. The simultaneous Boltzmann equations for a binary system are,

$$\left(\frac{\partial}{\partial t}+\mathbf{e}\cdot\nabla_{\mathbf{r}}+\mathbf{a}_{\mathbf{A}}\cdot\nabla_{\mathbf{e}}\right)f^{A}(\mathbf{r},\mathbf{e},t)=Q^{AA}+Q^{AB}, \tag{4.2}$$

$$\left(\frac{\partial}{\partial t}+\mathbf{e}\cdot\nabla_{\mathbf{r}}+\mathbf{a}_{\mathbf{B}}\cdot\nabla_{\mathbf{e}}\right)f^{B}(\mathbf{r},\mathbf{e},t)=Q^{BB}+Q^{BA}, \tag{4.3}$$

where $Q^{AB} = Q^{BA}$ is the collision integral that occurs due to the interactions among species *A* and *B*. With the *BGK* approximation [147], the collision integrals can be approximated by following linearized collision terms:

$$Q^{\sigma\sigma}=-\frac{1}{\lambda_{\sigma}}\left(f^{\sigma}-f^{\sigma(0)}\right) \tag{4.4}$$

$$Q^{\sigma s}=Q^{s\sigma}=-\frac{1}{\lambda_{\sigma s}}\left(f^{\sigma}-f^{\sigma s(0)}\right) \tag{4.5}$$

where σ represent one species (either *A* or *B*) and *s* represents the other one and λ is the relaxation parameter. The equilibrium distribution $f^{\sigma(0)}$ and $f^{\sigma s(0)}$ are generally taken to be the Maxwell-Boltzmann distribution for molecules.

The velocity space **e** can be discretized into a finite set of velocities $\{\mathbf{e}_{\alpha}\}$. Discretizing in time and space along a discretized velocity direction and expanding all the equilibrium distributions around the Maxwellian, we obtain the discrete Boltzmann equation on a lattice space or the lattice Boltzmann equation as follows,

$$f_{\alpha}^{\sigma}(\mathbf{r}_i+\mathbf{e}_{\alpha}\delta t,t+\delta t)-f_{\alpha}^{\sigma}(\mathbf{r}_i,t)=-\frac{1}{\tau_{\sigma}^{*}}\left[f_{\alpha}^{\sigma}(\mathbf{r}_i,t)-f_{\alpha}^{\sigma(0)}(\mathbf{r}_i,t)\right]-\frac{1}{\tau_{D}^{*}}\frac{\rho_s}{\rho}\frac{f_{\alpha}^{\sigma(eq)}}{R_{\sigma}T}(\mathbf{e}_{\alpha}-\mathbf{u})\cdot(\mathbf{u}_{\sigma}-\mathbf{u}_s)+\frac{\mathbf{a}_{\sigma}\cdot(\mathbf{e}_{\alpha}-\mathbf{u}_{\sigma})\delta t}{R_{\sigma}T}f_{\alpha}^{\sigma(0)}(\mathbf{r}_i,t) \tag{4.6}$$

where, ρ_{σ} and ρ_s, and $\mathbf{u}_{\sigma}$ and $\mathbf{u}_s$ are the mass densities and flow velocities for species σ and *s*. They are calculated from the moments of the distribution function,

$$\rho_\sigma = \sum_\alpha f_\alpha^\sigma = \sum_\alpha f_\alpha^{\sigma(0)} \quad \text{and} \quad \rho_\sigma \mathbf{u}_\sigma = \sum_\alpha f_\alpha^\sigma \mathbf{e}_\alpha = \sum_\alpha f_\alpha^{\sigma(0)} \mathbf{e}_\alpha \,. \tag{4.7a and b}$$

ρ and $\mathbf{u}$ are respectively, the mass density and the barycentric velocity of the mixture:

$$\rho = \rho_\sigma + \rho_s \quad \text{and} \quad \rho\mathbf{u} = \rho_\sigma \mathbf{u}_\sigma + \rho_s \mathbf{u}_s. \tag{4.8a and b}$$

The relaxation times τ_σ^* and τ_D^* are related to the fluid properties. Fluid viscosity is given by the relation $\nu_\sigma = \frac{1}{3}\left(\tau_\sigma^* - 0.5\right)\frac{\delta x^2}{\delta t}$, whereas, the mutual diffusivity is given by $D_{\sigma s} = \frac{\rho k_B T}{n m_\sigma m_s}\left(\tau_D^* - 0.5\right)\delta t$. Here, n is the number density of the molecules and m is the molecular mass of the species. For liquid we have assumed that the diffusivity does not depend on the molecular weight of the species. Hence, we have simplified the relation involving diffusivity by assuming same molecular weight of both the liquids, $D_{\sigma s} = \frac{1}{3}\left(\tau_D^* - 0.5\right)\frac{\delta x^2}{\delta t}$ [146].

In Eq. (4.7), $f_\alpha(\mathbf{r}_i,t)$ is the f distribution corresponding to the α^{th} discrete velocity $\mathbf{e}_\alpha$ and $f_\alpha^{\sigma(0)}$ and $f_\alpha^{\sigma(eq)}$ are the corresponding equilibrium distributions in the discrete velocity space. The equilibrium distributions in the corresponding directions are

$$f_\alpha^{\sigma(0)} = \left[1 + \frac{1}{R_\sigma T}\left(\mathbf{e}_\alpha - \mathbf{u}\right)\cdot\left(\mathbf{u}_\alpha - \mathbf{u}\right)\right] f_\alpha^{\sigma(eq)} \,. \tag{4.9}$$

$$f_\alpha^{\sigma(eq)} = \rho_\sigma w_\alpha \left[1 + \frac{1}{R_\sigma T}\left(\mathbf{e}_\alpha \cdot \mathbf{u}\right) + \frac{1}{2\left(R_\sigma T\right)^2}\left(\mathbf{e}_\alpha \cdot \mathbf{u}\right)^2 - \frac{1}{2R_\sigma T}\left(\mathbf{u}\cdot\mathbf{u}\right)\right]. \tag{4.10}$$

A popular lattice model is the two-dimensional nine-velocity (D2Q9) model (Fig. 2.1) for which the discrete velocities are

$$\mathbf{e}_\alpha = \left\{(0,0),\ \alpha = 0; \quad c\left\{\cos(\alpha-1)\frac{\pi}{4},\ \sin(\alpha-1)\frac{\pi}{4}\right\},\ \alpha = 1,3,5,7; \quad \sqrt{2}c\left\{\cos(\alpha-1)\frac{\pi}{4},\ \sin(\alpha-1)\frac{\pi}{4}\right\},\ \alpha = 2,4,6,8\right. \tag{4.11}$$

where $c = \sqrt{3R_\sigma T} = \delta x / \delta t$. The weights in Eq. (4.15) are

$$w_\alpha = \begin{cases} \frac{4}{9}, \alpha = 0; & \frac{1}{9}, \alpha = 1,3,5,7; & \frac{1}{36}, \alpha = 2,4,6,8 \end{cases}. \quad (4.12)$$

4.3.2 Boundary Conditions

At the two walls no-slip boundary condition is applied as proposed by Zou and He [96]. The boundary condition is based on bounce back of the non-equilibrium part of those distribution functions *f*, which are perpendicular to the wall. Therefore following the notations of Fig. 2.1,

$$f_3^{neq} = f_7^{neq} \text{ and } f_1^{neq} = f_5^{neq} \quad (4.13a \text{ and } b)$$

for horizontal and vertical walls respectively.

For this boundary condition wall velocities are specified while the density and the unknown *f* distributions are calculated by using Eqs. (4.9), (4.10) and (4.8a and b).

For inlet boundary condition, we know all the information regarding velocity and density. Similarly, at the outlet, we have used extrapolation scheme to predict the density and the x-component of velocity, *u*. The y-component of velocity, *v* is assumed to be zero. As, all the velocities and densities are known; we have used the equilibrium distribution of the unknown *f*'s as the boundary condition. For inlet, the unknown *f*'s are f_1, f_2 and f_8 while for outlet, those are f_4, f_5 and f_6.

4.3.3 Magnetic Body Force

The coflow of the magnetic and non-magnetic fluids in a channel is governed by the continuity and Navier-Stokes equations (which include the magnetic body force or Kelvin body force), i.e.,

$\nabla.\mathbf{u} = 0$, and $\rho\frac{\partial \mathbf{u}}{\partial t} + \rho\mathbf{u}\cdot\nabla\mathbf{u} = -\nabla p + \mu\nabla^2\mathbf{u} + (\mathbf{M}.\nabla)\mathbf{B}$, (4.14a and b)

The Kelvin body force $(\mathbf{M}.\nabla)\mathbf{B}$ depends upon magnetization $\mathbf{M} = \phi \mathrm{M_{sat}}\left(\coth\alpha - \frac{1}{\alpha}\right)\frac{\mathbf{H}}{\mathrm{H}}$.

Here the Langevin's parameter [148] is given by $\alpha = \frac{4}{3}\pi \mathrm{a}^3 \frac{\mu_0 \mathrm{M_{sat}}}{\mathrm{k_B T}}\mathrm{H}$ and M_{sat} denotes the saturation magnetization, a represents the particle diameter, μ_0 the magnetic permeability of vacuum, k_B the Boltzmann constant and T the temperature. The magnetic field is given by $\mathbf{B} = \mu_0(\mathbf{M}+\mathbf{H})$, where the imposed magnetic field due to a magnetic line dipole of strength m is given by $\mathbf{H} = \frac{m}{r^2}\left(\sin\phi\mathbf{e}_r - \cos\phi\mathbf{e}_\phi\right)$, and (r, ϕ) denotes the coordinate of any point with the origin at the magnetic dipole [148].

4.4 Results and Discussions

In our simulations, both fluids are introduced at a uniform velocity U, the flow Reynolds number for each fluid based on the microchannel half width $\mathrm{Re} = \rho U h/2\nu = 1$, and the microchannel length $L = 25h$. For simplicity, both fluids are assumed to have same density ρ and viscosity ν. The two magnets are placed across the microchannel (cf. Fig. 4.1) at distances $r/h = 2.4$ away from the microchannel walls and at a distance $s/h = 3$ apart from each other. The first magnet is located at a $6h$ axial displacement from the microchannel inlet so that its magnetic field does not affect the inlet flow. Its strength m is such that the magnetic pressure number, which is the ratio of the magnetic and inertia forces, $M_P = \frac{\mu_0 \phi M_{sat} m}{\rho U^2 h^2} = 5.17\times10^5$. The values of various parameters used in the simulations are provided in Table 4.1.

Table 4.1: Values of various parameters used for simulating magnetic assisted mixing.

Parameters	**Values**
Density, ρ	1000 kg/m^3
Viscosity, ν	1×10^{-6} m^2/s
Channel width, h	50×10^{-6} m
Saturation magnetization, M_{sat}	4.46×10^{5} A/m
Absolute permeability, μ_0	$4\pi\times10^{-7}$ N/A^2
Particle volume fraction, ϕ	0.03

In the absence of the magnetic field, mixing occurs through pure diffusion alone. To assess the viability of the imposed technique, we compare magnetically assisted mixing with the purely diffusive mixing. Figure 4.2 presents the concentration of the magnetic fluid for both cases at the same dimensionless time, where time is normalized with the convection time $t_{conv} = h/U$. It is apparent that magnetic assisted mixing is enhanced in comparison to pure diffusion. For the purely diffusive case, mixing is essentially limited to regions close to the interface. Reasonable mixing is achieved at further downstream distances. In the presence of a magnetic field, the ferrofluid undergoes a crisscross motion that results in two vortices, which enhances mixing. In this case, good mixing is achieved even at locations close to the inlet with the exception of a few unmixed islands.

We quantify mixing at any plane along the microchannel through a mixing index $M = 1 - \frac{\sigma}{\sigma_0}$ [149], where

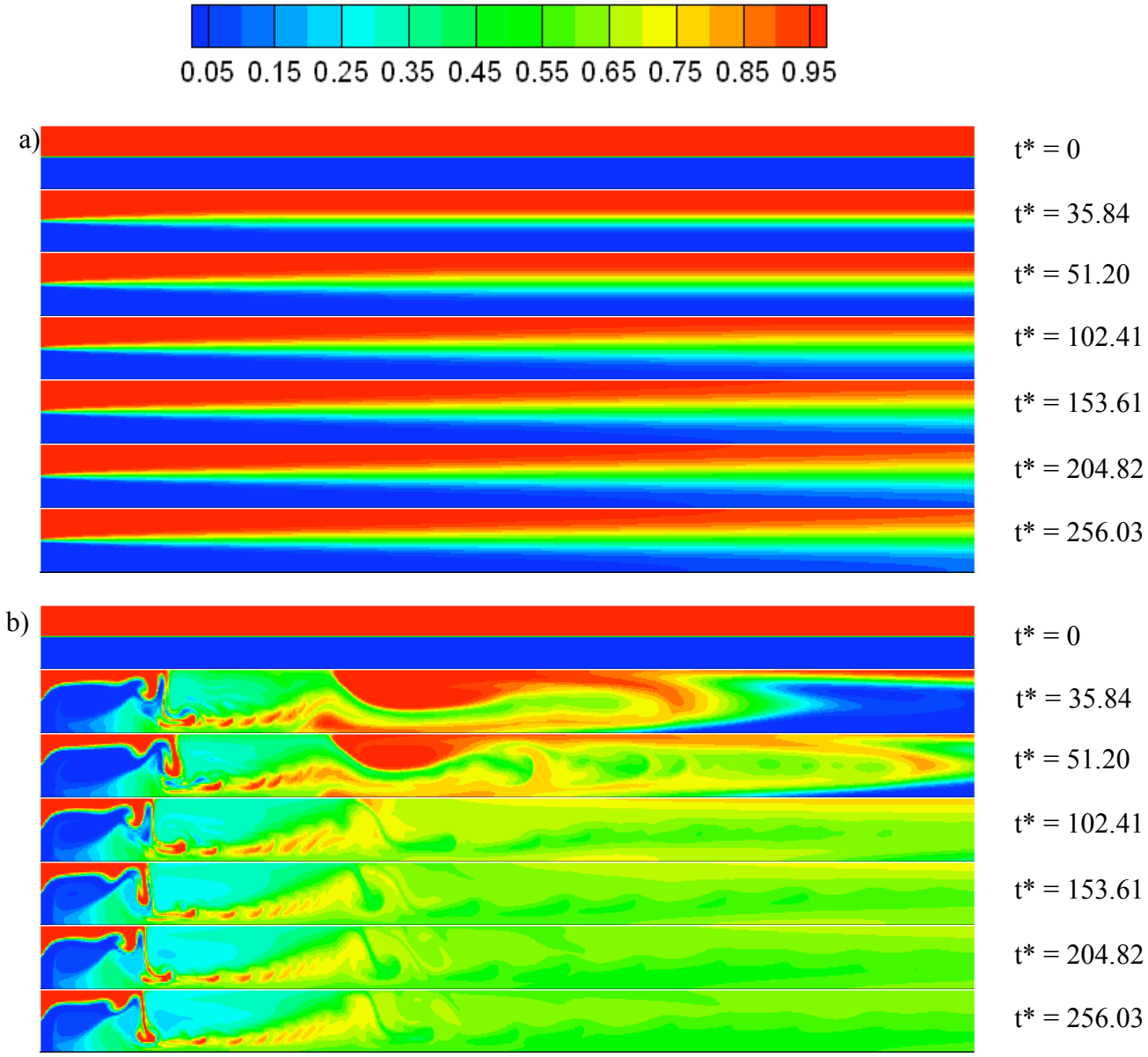

Figure 4.2. Magnetic fluid concentration contours in a microchannel at different times for Sc = 1000, Re = 1: (a) pure diffusive mixing; and (b) magnetic assisted mixing with $M_p = 5.17\times10^5$ and $r/h = 2.4$, $s/h = 3$.

$$\sigma^2 = \frac{1}{N}\sum_{i=1}^{N}\left(C_i - C_0\right)^2 \tag{15}$$

denotes the variance of the instantaneous concentration distribution, σ_0^2 the variance of a reference distribution, C_i the concentration of one of the two species at the i^{th} node, C_o the reference concentration of that species, and N the number of nodes in that plane [150]. For an open system such as microchannel in which mixing progresses as the fluid moves axially, we follow the customary procedure of taking the initial inlet distribution as the reference to normalize the results and calculate σ_0 [151]. The value of C_0 is defined by the average concentration of the fluid at any instant along a specified transverse plane.

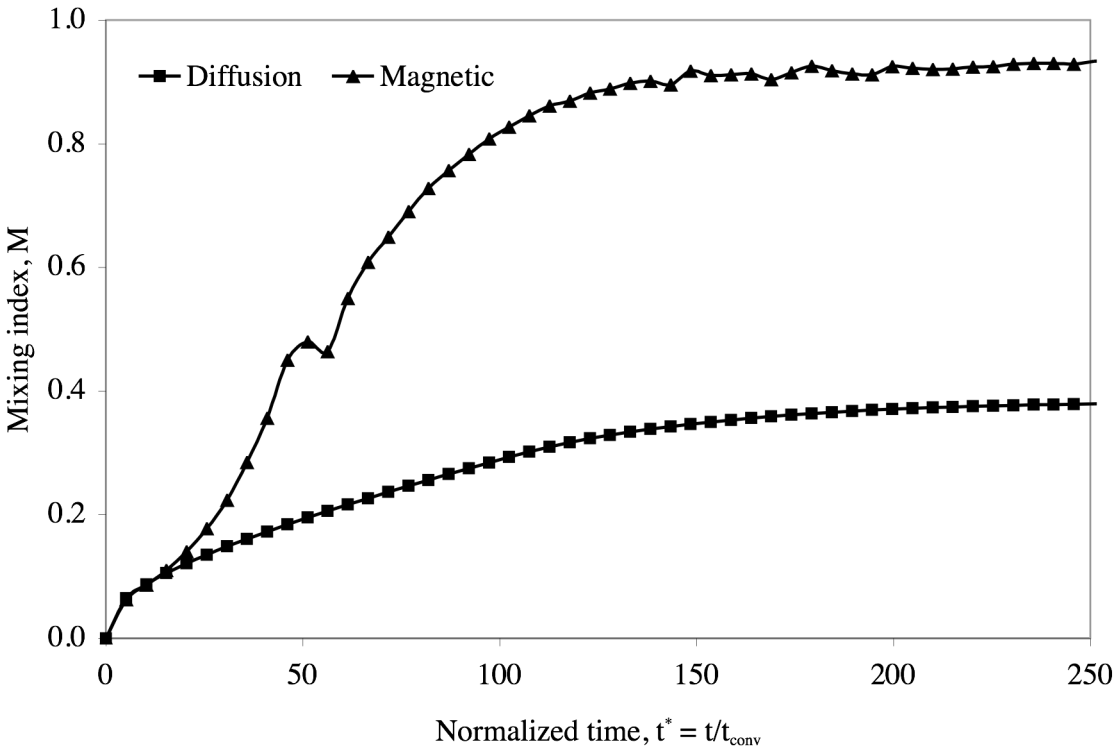

Figure 4.3. Temporal variation of the mixing index M for pure diffusive mixing and magnetic assisted mixing for the conditions of Fig. 4.2.

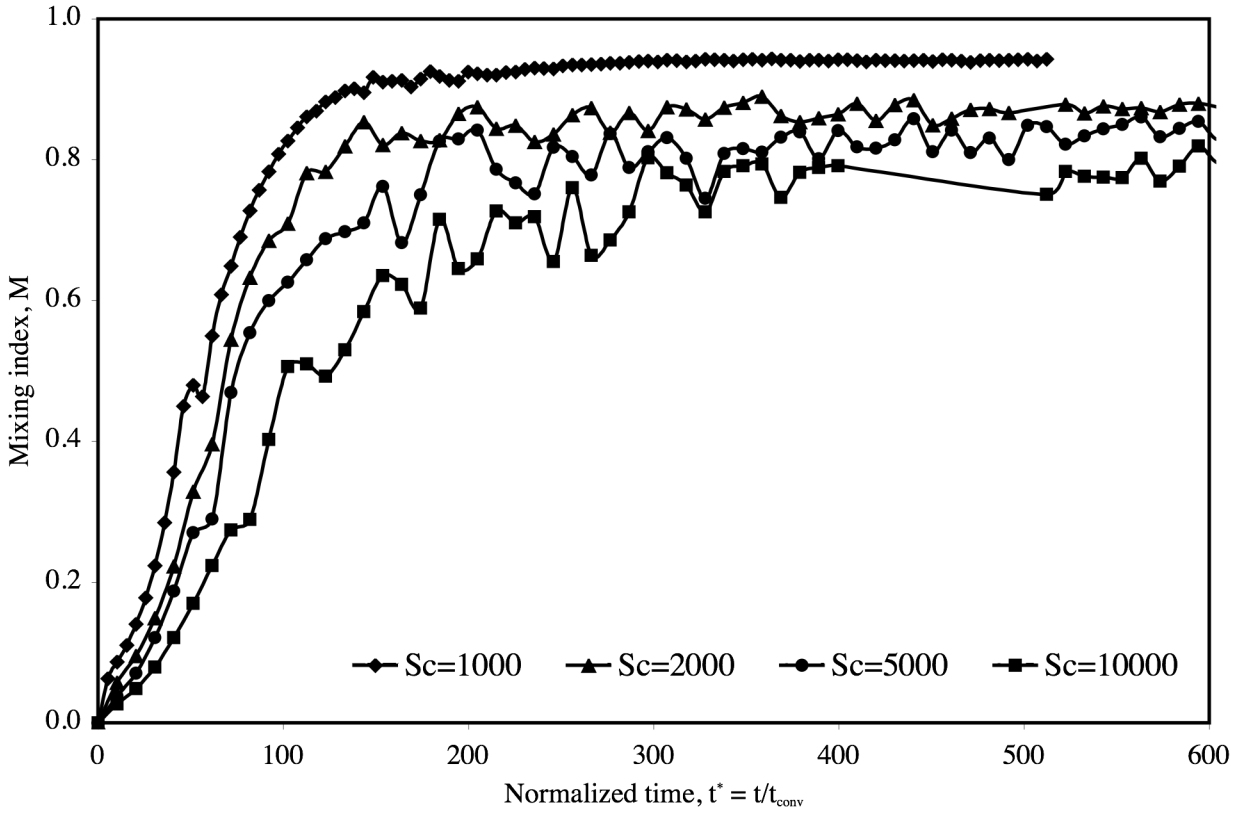

Figure 4.4. Temporal variation of the mixing index with Schmidt number for magnetic assisted mixing for the conditions of Fig. 4.2.

Thus, M = 1 for perfect mixing and M = 0 for a totally unmixed condition.

The temporal variation of M at the microchannel outlet for purely diffusive and magnetic assisted mixing, with the same initial conditions for both cases, is presented in Fig. 4.3. As expected, the value of M increases more rapidly during magnetic assisted mixing than for pure diffusive mixing. For magnetic assisted mixing, the mixing index increases to an equilibrium value of 0.94, while for diffusive mixing the corresponding value of M ~ 0.37. For magnetic-induced mixing, M increases very steeply initially, reaching a value of ~ 0.8 within t=100. However, the subsequent increase in M is rather slow and comparable to that for diffusive mixing. A review of the concentration contours

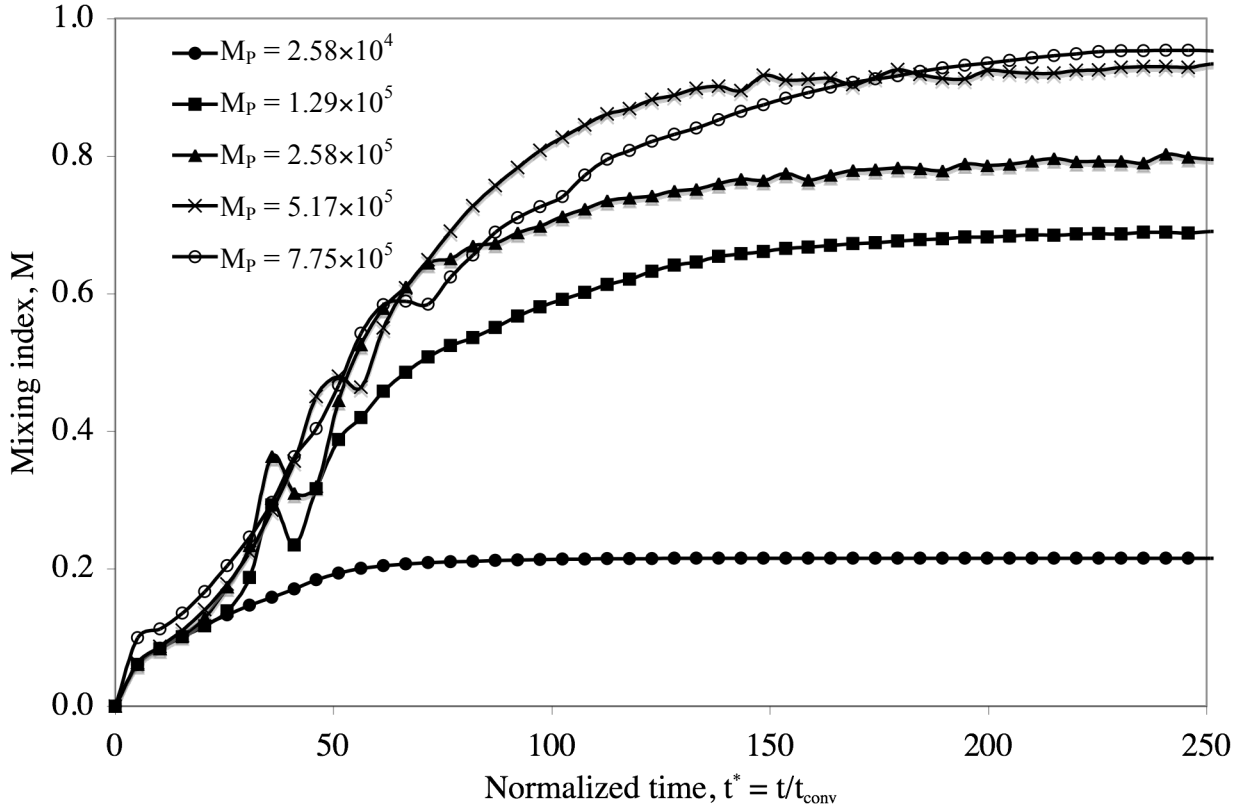

Figure 4.5. Temporal variation of the mixing index for various values of the magnetic pressure number for the conditions of Fig. 4.2.

in Fig. 4.2 shows that when $t^*>100$, there are concentration inhomogeneities at the exit plane over small regions close to the wall. In these regions, as the length scale decreases, diffusion becomes increasingly dominant over advection. Hence, the mixing during these later times occurs primarily through diffusion, which explains the slow mixing at the end of the channel.

Next, we compare the M values obtained during magnetic assisted mixing for various Schmidt numbers $Sc = \nu/D$ (that denote the ratio of the momentum to mass diffusivities) with respect to the normalized mixing time $t^* = t/t_{conv}$ in Fig. 4.4 for four cases (Sc = 1000, 2000, 5000 and 10000) with M calculated at the microchannel outlet ($x = 40h$). For all cases, Re = 1, and $M_P = 5.17\times10^5$ (with the dipoles placed at $r/h = 2.4$ and

s/*h* = 3). As seen through Fig. 4.3, diffusion plays an important role during the final stages of mixing. Thus for Sc = 10000, when the diffusivity is very small, M cannot increase beyond the advectively achieved limit of ~ 0.8. The value of M decreases with increasing Sc; for Sc = 1000, M = 0.96 while for Sc = 10000, M = 0.8. This is expected, since increasing Sc implies a decreasing influence of molecular diffusivity. Consequently, the contribution of molecular diffusion to mixing is reduced, leading to an increase in the time required to achieve a specified level of mixing. Changes in the rapidity of mixing are very small over a relatively large Sc range, since the time required for M to reach a steady state is almost unchanged (c.f. Fig. 4.3).

The strength of the magnetic field is changed by altering *m* or by modifying the magnet placements through varying *r*. First, we investigate the effect of varying *m* while keeping the other parameters constant (Re = 1, Sc = 1000, *r*/*h* = 2.4, *s*/*h* = 3, and L = 25*h*). An increase in *m* also increases M_P. Fig. 4.5 presents the time evolution of M at the end of the microchannel for varying M_P and shows that mixing improves with increasing M_P. When M_P is small, the magnetic field is too weak to influence the axial movement of the magnetic fluid and deflect it crosswise. For these cases, mixing occurs primarily due to diffusion, resulting in a much lower equilibrium value, e.g., M ≈ 0.21 for M_P = 2.58×10^4. This mixing index value is even smaller than for pure diffusive mixing for which M ≈ 0.37. In this case, the magnet placed near the top wall, although weak, holds the magnetic fluid and prevents it from diffusing away, which is counterproductive for mixing. With increasing M_P, the magnetic field strength increases, but the vortex motion also becomes stronger. Thus, the increasing cross-stream motion overcomes the limited

diffusion of the magnetic fluid and results in larger equilibrium values of M. For, M_p = 7.75×10^5, M ≈ 0.963.

Next, the influence of varying *r* is investigated. Fig. 4.6 presents the temporal variation of M for various values of *r*/*h* with the other parameter values maintained constant as above, and $M_p = 2.58\times10^5$. The equilibrium value of M increases with decreasing *r*/*h* (or decreasing *r* as the magnet is brought closer to the wall), resulting in better mixing. As *r*/*h* decreases, the magnetic field strength increases and the vortex rolls strengthen. For larger values, e.g., *r*/*h* = 8, the magnetic field acting on the fluid is so

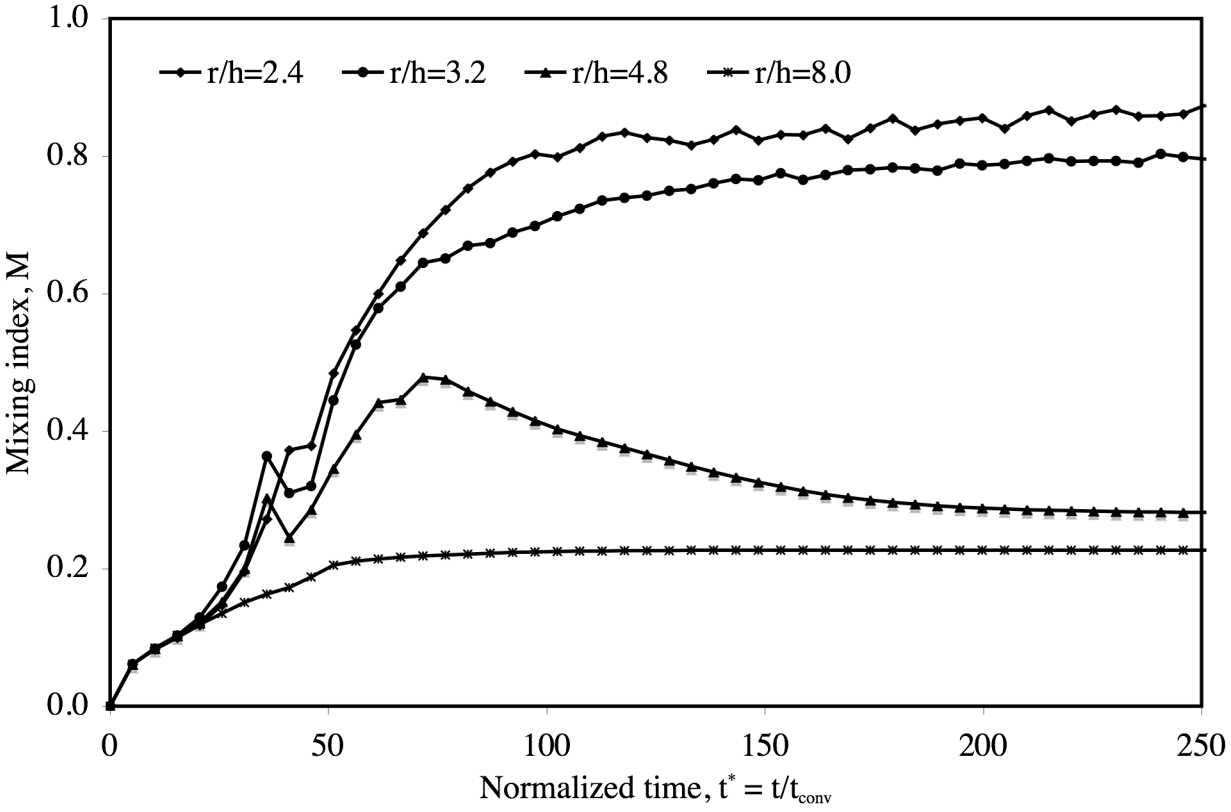

Figure 4.6. Temporal variation of the mixing index for various values of *r*/*h*, where *r* denotes the distance of the magnet from the microchannel wall for the conditions of Fig. 4.2.

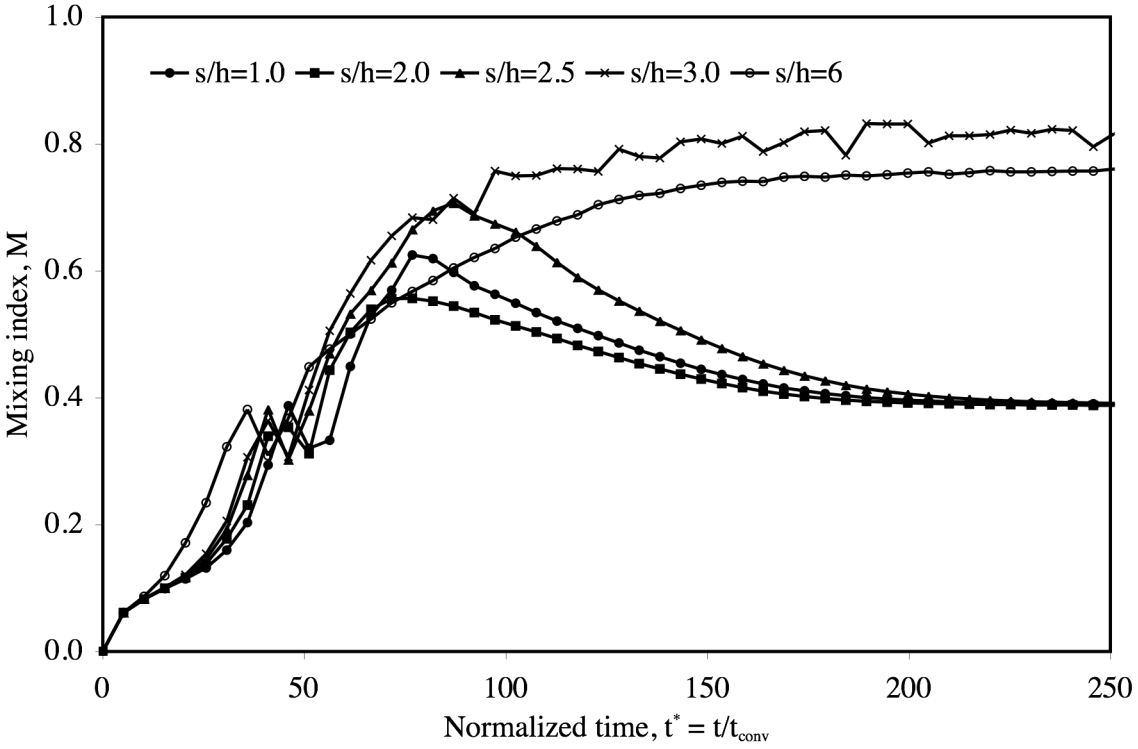

Figure 4.7. Temporal variation of the mixing index for various values of *s/h*, where *s* denotes the distance between two magnets for the conditions of Fig. 4.2.

weak that it cannot induce effective cross-stream motion. Consequently, mixing occurs primarily due to diffusion and so, again, at equilibrium M ≈ 0.23.

Mixing is also dependent on the separation distance *s* between the magnets as shown in Fig. 4.7, with all other parameters maintained as above. If the magnets are placed very close to each other ($s/h \leq 2.5$), the mixing, and thus the equilibrium value of M, diminishes. For closely placed magnets, the equilibrium value of M ≈ 0.39, while M ≈ 0.81 when the ratio *s/h* is larger. Fig. 4.8 contains contour plots of the magnetic fluid concentration and velocity for $s/h = 2.5$ and $s/h = 3.0$. For the latter case (Fig. 4.8a), the magnetic fluid generates two vortex rolls that do not interact with each other but maintain

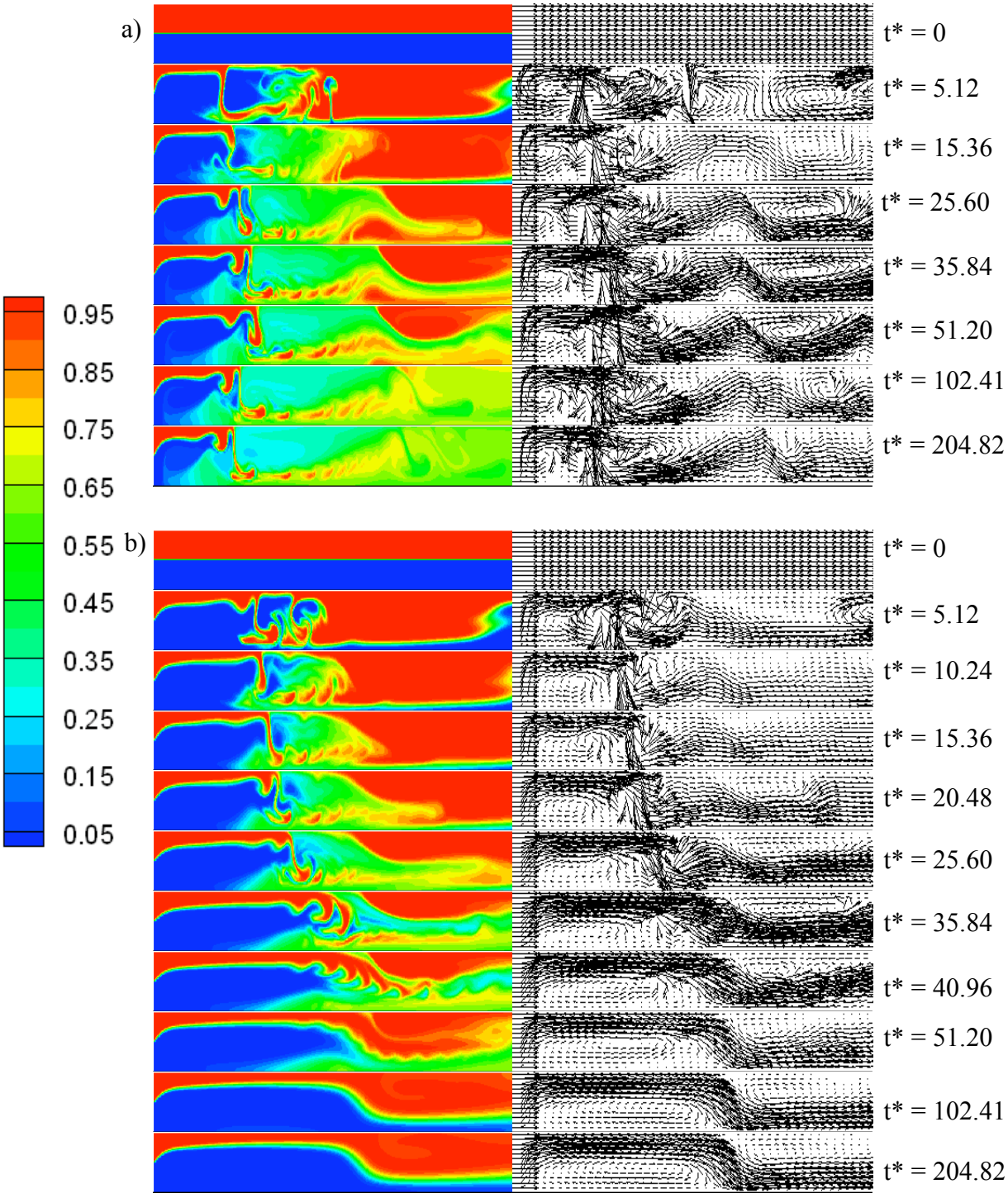

Figure 4.8. Magnetic fluid concentration contours and the corresponding velocity vectors for the microchannel flow at different times for the conditions of Fig. 4.2: (a) $s/h = 2.5$; and (b) $s/h = 3.0$.

their existence. When s/h = 2.5 (Fig. 4.8b), these rolls form very close to each other, which helps to generate some initial mixing. However, since the rolls now interact, they merge and cease to exist after $t^* = 40.96$, leading to simple streamwise motion resembling the flow over an obstacle, which has been previously noted for magnetic fluids [152]. After $t^* = 41$, the vortices diminish in strength so that the ferrofluid agglomerates near the top magnet forming an obstacle. The remaining fluid must negotiate that agglomerate. While there are still two small vortices close to that wall inducing fluid rotation in that region alone, these small vortex rolls do not assist in fluid mixing since the two fluids are separated.

CHAPTER 5

CONCLUSIONS AND FUTURE REEARCH DIRECTIONS

5.1 Conclusions

The salient conclusions for the electroosmotic mixing and magnetic assisted mixing are summarized as follows:

5.1.1 Electroosmotic Mixing

Electroosmotic mixing in a microscale cavity is studied by using lattice Boltzmann method (LBM). In contrast to the common practice of complex potential distribution and transient electric field, rapid and efficient mixing is achieved by using homogeneous zeta potential and steady electric field. Stokes flow through a microchannel can be considered as the result of the superposition of a one-dimensional axial flow upon the two-dimensional transverse flow along any of its cross sections. We have simulated the corresponding two dimensional transverse electroosmotic flow (EOF) using LBM. Instead of the commonly used Helmholtz-Smoluchowski (H-S) slip velocity formulation, electric double layer is spatially resolved to determine the local EOF velocity. The simulations show that rapid maxing can be achieved by using a homogeneous zeta potential and a steady electric field. The quality of mixing depends on the choice of wall, which is provided with a zeta potential and the corresponding direction of the electric field. Mixing is enhanced when a zeta potential is imparted to the channel wall that is perpendicular to the initial particle distribution and when an electric field is also applied along the direction of this potential. The rapidity of mixing can be characterized by a

normalized time that depends upon the electro-osmotic time scale. In general, a stronger electric field induces more rapid mixing. Under some configurations, the mixing time for water-soluble organic molecules can even be reduced by four orders of magnitude. The mixing rate is found to follow a unique relation for any particular configuration, which depends on viscosity and permittivity of the medium as well as the electric field strength and the dimension of the cavity.

5.1.2 Magnetic Assisted Mixing

A multicomponent lattice Boltzmann method is developed to study the effect of magnetic body force on the ferrofluid. A novel mixing scheme is proposed to utilize the effect of magnetic field on te ferrolfuid in order to enhance mixing in a microchannel. Two fluids, one of them is magnetic, are introduced in the channel when two magnets are placed across the microchannel at some axial distance apart. In presence of the interacting magnetic field, the magnetic fluid tries to follow a zig-zag motion and generates two rolls of votices, thereby enhances mixing. While magnetic assisted mixing is more rapid than that attributable to pure diffusion alone, decreasing the Schmidt number (or increasing the diffusivity) also improves the mixing between the two fluids, particularly during the later stages of the microchannel flow. However, the time required to achieve an equilibrium value of the mixing index does not change significantly with varying Schmidt number. Magnetic assisted mixing improves as the magnetic field strength increases, e.g., by raising the dipole strength or reducing the distance between the dipole and the microchannel wall. However, if the dipole strength is significantly lowered, the magnetic field is unable to generate the vortex pair required to enhance mixing. Instead, the magnet that lies closer to the magnetic fluid attracts it, preventing its diffusion, so that

the mixing rate for such a case is even lower than for pure diffusion. When the axial distance between the magnet pair is brought closer than a critical distance, the two vortex rolls interact and merge into a single vortex, resulting in the local accumulation of the ferrofluid. However, the exact reason behind this phenomenon is yet to be explored.

5.2 Future Research Directions

Current research concentrates on the numerical modeling of the microchannel flows and microscale mixing. The nature of this research is exploratory and shows the proof of the concept. However, implementation of these schemes in the actual microfluidic device requires detail experimentations. Benchmark experiments in the similar configurations are proposed as the next level of study. The parameters used in the current investigations would serve as the design bases of the experiments.

The numerical study of magnetic assisted mixing assumes no-slip boundary condition at the channel wall. However, the effect of magnetic body force becomes more prominent with decreasing length scale, when no-slip condition becomes no longer valid. The future numerical studies should involve the effect of wall slip on the ferrofluid flow thorugh channel. The ferrofluid is assumed to be a very dilute suspension of magnetic nanoparticles. The fluid behavior will be different if the particle concentration is increased. Therefore, particles should be modeled as a separate phase in such situation.

Magnetic fluid has a potential for various other applications. It is found that if magnetic particles are exposed to alternate magnetic field, there is a loss of magnetic energy, which generates heat and increases the temperature of the medium and the surrounding. Living cells and organs are very sensitive to its environment temperature. It is observed that certain tumor and cancer cells die if the surrounding temperature is

increased beyond a critical value. This phenomenon is known as hyperthermia. Magnetic fluid can be used as a localized heating agent to kill infected tumor and cancer cells. It can be localized at a particular location with the help of a magnet and can generate controlled heating at the desired location. The targeted heating can localize the effect only at the location of interest and prevents the adverse side effects. The magnetic heating can be modeled by using thermal lattice Boltzmann method. It requires a proper modeling of the heat generation due to the alternate magnetic field. A parametric study should be performed to characterize the effect of field strength and frequency of the alternate field on the heating. The blood flow surrounding the magnetic fluid can cause heat dissipation. Therefore, a parametric study of the effect of blood flow Reynolds number and Womersely number on the heat generation is also recommended.

REFERENCES

1 Seong, G. H. and Crooks, R. M., Efficient mixing and reactions within microfluidic channels using microbead-supported catalysts, *J. Am. Chem. Soc.* **124** 13360 (2002).

2 Chou, H., Spence, C., Scherer, A. and Quake, S. R., A microfabricated device for sizing and sorting DNA molecules, *Proc. Natl. Acad. Sci. U.S.A.* **96** 11 (1999).

3 Burns, M. A., Johnson, B. N., Brahmasandra, S. N., Handique, K., Webster, J. R., Krishnan, M., Sammarco, T. S., Man, P. M., Jones, D., Heldsinger, D., Mastrangelo, C. H. and Burke, D. T., An integrated microfabricated DNA analysis device, *Science*, **282** 484 (1998).

4 Losey, M. W., Jackman, R. J., Firebaugh, S. L., Schmidt, M. A. and Jensen, K. F., Design and fabrication of microfluidic devices for multiphase mixing and reaction, *J. Microelectromech. Syst.*, **11** 709 (2002).

5 Burns, J. R. and Ramshaw, C., The intensification of rapid reactions in multiphase systems using slug flow in capillaries, *Lab Chip*,**1** 10 (2001).

6 Manz, A., Graber, N. and Widmer, H. M., Miniaturized total chemical analysis systems: A novel concept for chemical sensing, *Sensors Actuators,* **1** 244 (1990).

7 Greenwood, P. A. and Greenway, G. M., *Trends Anal. Chem.*, **21** 726 (2002).

8 Shaikh, K. A., Ryu, K. S., Goluch, E. D., Nam, J. M., Liu, J. W., Thaxton, S., Chiesl, T. N., Barron, A. E., Lu, Y., Mirkin, C. A. and Liu, C., A modular microfluidic architecture for integrated biochemical analysis, *Proc. Natl. Acad. Sci. U.S.A.*, **102** 9745 (2005).

9 Auroux, P. A., Iossifidis, D., Reyes, D. R. and Manz, A., Micrototal analysis systems. 2. Analytical standard operations and applications, *Anal. Chem.*, **74** 2637 (2002).

10 Ionescu-Zanetti, C., Shaw, R. M., Seo, J. G., Jan, Y. N., Jan, L. Y. and Lee, L. P., Mammalian electrophysiology on a microfluidic platform, *Proc. Natl. Acad. Sci. U.S.A.*, **102** 9112 (2005).

11 Fredrickson, C. K. and Fan, Z. H., Macro-to-micro interfaces for microfluidic devices, *Lab Chip*, **4** 526 (2004).

12 Hertzog, D. E., Michalet, X., Jaeger, M., Kong, X. X., Santiago, J., Weiss, S. and Bakajin, O., Microsecond mixer for kinetic studies of protein folding, *Biophysical J.*, **88** 376A (2005).

13 Song, H., Tice, J. D. and Ismagilov, R. F., A Microfluidic System for Controlling Reaction Networks in Time*, Angew. Chem. Int. Ed.*, **42** 768 (2003).

14 Rohr, T., Yu, C., Davey, M. H., Svec, F. and Frechet, J. M. J., Porous polymer monoliths: Simple and efficient mixers prepared by direct polymerization in the channels of microfluidic chips, *Electrophoresis*, **22** 3959 (2001).

15 Jeon, S., Malyarchuk, V., White, J. O. and Rogers, J. A., Optically fabricated three dimensional nanofluidic mixers for microfluidic devices, *Nano Lett.*, **5** 1351 (2005).

16 Kakuta, M., Bessoth, F. G. and Manz, A., Microfabricated devices for fluid mixing and their application for chemical synthesis, *Chem. Rec.*, 1 395 (2001).

17 Jiang, F., Drese, K. S., Hardt, S., Küpper, M. and Schönfeld, F., Helical flows and chaotic mixing in curved micro channels, *Amer. Inst. Chem. Engg. J.*, **50** 2297 (2003).

18 Kenis, P. J. A., Ismagilov, R. F. and Whitesides, G. M., Microfabrication inside capillaries using multiphase laminar flow patterning, *Science*, **285** 83 (1999).

19 Strook, A. D., Dertinger, S. K. W., Ajdari, A., Mezi, I., Stone, H. A. and Whitesides, G. M., Chaotic mixer for microchannel, *Science*, **295** 647 (2000).

20 Liu, R. H., Stremler, M. A., Sharp, K. V., Olsen, M. G., Santiago, J. G., Adrian, R. J., Aref, H. and Beebe, D.J., Passive mixing in a three-dimensional serpantine microchannel, *J. Microelectromech. Syst.*, **9** 190 (2000).

21 Kamholz, A. E.,Weigl, B. H., Finlayson, B. A. & Yager, P. Quantitative analysis of molecular interaction in a microfluidic channel: the T-Sensor, *Anal. Chem.*, **71** 5340 (1999).

22 Kamholz, A. E. and Yager, P., Molecular diffusive scaling laws in pressure-driven microfluidic channels: deviation from one-dimensional Einstein approximations, *Sensors Actuators B*, **82** 117 (2002).

23 Ismagilov, R. F., Stroock, A. D., Kenis, P. J. A., Whitesides, G. and Stone, H. A., Experimental and theoretical scaling laws for transverse diffusive broadening in two-phase laminar flows in microchannels, *Appl. Phys. Lett.*, **76** 2376 (2000).

24 Yi, M. and Bau, H. H., The kinematics of bend-induced mixing in micro-conduits, *Int. J. Heat Fluid Flow*, **24** 645 (2003).

25 Wong, S. H., Ward, M. C. L. and Wharton, C. W., Micro T-mixer as a rapid mixing micromixer, *Sensors Actuators B*, **100** 365 (2004).

26 Branebjerg, J., Graveson, P., Krog, J. and Nielsen, C., Fast mixing by lamination, *Proc. MEMS '96, 9th IEEE Int. Workshop on Micro Electro Mechanical Systems, (San Diego, CA)* 441 (1996).

27 Schwesinger, N., Frank, T. and Wurmus, H., A modular microfluidic system with an integrated micromixer, *J. Micromech. Microeng.*, **6** 99 (1996).

28 Gray, B. L., Jaeggi, D., Mourlas, N. J., van Drieënhuizen, B. P., Williams, K. R., Maluf, N. I. and Kovacs, G. T. A., Novel interconnection technologies for integrated microfluidic systems, *Sensors Actuators A*, **77** 57 (1999).

29 Munson, M. S. and Yager, P., Simple quantitative optical method for monitoring the extent of mixing applied to a novel microfluidic mixer, *Anal. Chim. Acta.,* **507** 63 (2004).

30 He, B., Burke, B. J., Zhang, X., Zhang, R. and Regnier, F. E., A picoliter-volume mixer for microfluidic analytical systems, *Anal. Chem.*, **73** 1942 (2001).

31 Melin, J., Gimenez, G., Roxhed, N., van der Wijngaart, W. and Stemme, G., A fast passive and planar liquid sample micromixer, *Lab Chip*, **4** 214 (2004).

32 Miyake, R., Lammerink, T. S. J., Elwenspoek, M. and Fluitman, J. H. J., Micromixer with fast diffusion, *Proc. MEMS '93, 6th IEEE Int. Workshop Micro Electro Mechanical System (San Diego, CA)* 248 (1993).

33 Miyake, R., Tsuzuki, K., Takagi, T., Imai, K., A highly sensitive and small flow-type chemical analysis system with integrated absorbtionmetric micro-flowcell, *Proc. MEMS'97, 10th IEEE Int. Workshop Micro Electro Mechanical System (Nagoya, Japan)*, 102 (1997).

34 Larsen, U. D., Rong, W. and Telleman, P., Design of rapid micromixers using CFD, *Proc. Transducers'99, 10th Int. Conf. on Solid-State Sensors Actuators (Sendai, Japan)*, 200 (1999).

35 Seidel, R. U., Si, D. Y., Menz, W. and Esashi, M., Capilary force mixing device as sampling module for chemical analysis, *Proc. Transducers'99, 10th Int. Conf. on Solid-State Sensors Actuators (Sendai, Japan)*, 438 (1999).

36 Voldman, J., Gray, M. L. and Schmidt, M. A., An integrated liquid mixer/valve, *J. Microelectromech. Syst.*, **9** 295 (2000).

37 Wang, H., Iovenitti, P., Harvey, E. and Masood, S., Optimizing layout of obstacles for enhanced mixing in microchannels, *Smart Mater. Struct.*, **11** 662 (2002).

38 Lin, Y., Gerfen, G. J., Rousseau, D. L. and Yeh, S. R., Ultrafast microfluidic mixer and freeze-quenching device, *Anal. Chem.*, **75** 5381 (2003).

39 Hong, C. C., Choi, J. W. and Ahn, C. H., A novel in-plane microfluidic mixer with modified tesla structures, *Lab Chip*, **4** 109 (2004).

40 Liu, R. H., Stremler, M. A., Sharp, K. V., Olsen, M. G., Santiago, J. G., Adrian, R. J., Aref, H. & Beebe, D. J., Passive mixing in a three-dimensional serpentine microchannel, *J. Microelectromech. Syst.*, **9** 190 (2000).

41 Johnson T. J., Ross D. and Locascio L. E., Rapid microfluidic mixing, *Anal. Chem.*, **74** 45 (2002).

42 Stroock, A. D., Dertinger, S. K., Ajdari, A., Mezic, I., Stone, H. A. and Whitesides, G. M., Chaotic mixer for microchannels, *Science*, **295** 647 (2002).

43 Stroock, A. D. and Whitesides, G. M., Controlling flows in microchannels with patterned surface charge and topography, *Acc. Chem. Res.*, **36** 597 (2003).

44 Wang, H., Iovenitti, P., Harvey, E. and Masood, S., Numerical investigation of mixing in microchannels with patterned grooves, *J. Micromech. Microeng.*, **13** 801 (2003).

45 Kim, D. S., Lee, S. W., Kwon, T. H. and Lee, S. S., A barrier embedded chaotic micromixer *J. Micromech. Microeng.*, **14** 798 (2004).

46 Hosokawa, K., Fujii, T. and Endo, I. 1999 Droplet-based nano/picoliter mixer using hydrophobic microcapillary vent, *Proc. MEMS'99, 12th IEEE Int. Workshop Micro Electro Mechanical System (Piscataway, NJ)*, 388 (1999).

47 Handique, K. and Burns, M. A., Mathematical modeling of drop mixing in a slit-type microchannel, *J. Micromech. Microeng.*,**11** 548 (2001).

48 Paik, P., Pamula, V. K. and Fair, R. B., Rapid droplet mixers for digital microfluidic systems, *Lab Chip*, **3** 253 (2003).

49 Song, H., Bringer, M. R., Tice, J. D., Gerdts, C. J. and Ismagilov, R. F., Experimental test of scaling of mixing by chaotic advection in droplets moving through microfluidic channels, *Appl. Phys. Lett.*, **83** 4664 (2003).

50 Tice, J. D., Lyon, A. D. and Ismagilov, R. F., Effects of viscosity on droplet formation and mixing in microfluidic channels, *Anal. Chim. Acta.*, **507** 73 (2003).

51 Lu, L.-H., Ryu, K. S. and Liu, C., A magnetic microstirrer and array for microfluidic mixing, *J. Microelectromech. Syst.*, **11** 462 (2002).

52 Liu, R. H., Lenigk, R., Druyor-Sanchez, R. L., Yang, J. N. and Grodzinski, P., Hybridization enhancement using cavitation microstreaming, *Anal. Chem.*, **75** 1911 (2003).

53 Oddy, M. H., Santiago, J. G. and Mikkelsen, J. C., Electrokinetic instability micromixing, *Anal. Chem.*, **73** 5822 (2001).

54 Glasgow, I. and Aubry, N., Enhancement of microfluidic mixing using time pulsing, *Lab Chip*, **3** 114 (2003).

55 Thorsen, T., Maerkl, S. J., and Quake, S. R., Microfluidic large-scale integration, *Science*, **298** 580 (2002).

56 Deshmukh, A. A., Liepmann, D. and Pisano, A. P., Continuous micromixer with pulsatile micropumps, *Tech. Digest IEEE Solid State Sensor and Actuator Workshop (Hilton Head Island, SC)*, 73 (2000).

57 Deshmukh, A. A., Liepmann, D. and Pisano, A. P., Characterization of a micro-mixing, pumping, and valving system, *Proc. Transducers'01, 11th Int. Conf. on Solid-State Sensors Actuators (Munich, Germany)*, 779 (2001).

58 Fujii, T., Sando, Y., Higashino, K. and Fugii, Y., A plug and play microfluidic device, *Lab Chip*, **3** 193 (2003).

59 Glasgow, I. and Aubry, N., Enhancement of microfluidic mixing using time pulsing, *Lab Chip*, **3** 114 (2003).

60 Niu, X. Z. and Lee, Y. K., Efficient spatial–temporal chaotic mixing in microchannels, *J. Micromech. Microeng.*, **13** 454 (2003).

61 Evans, J., Liepmann, D. and Pisano, A. P., Planar laminar mixer, *Proc. MEMS'97, 10th IEEE Int. Workshop Micro Electro Mechanical System (Nagoya, Japan)*, 96 (1997).

62 Okkels, F. and Tabeling, P., Spatiotemporal resonances in mixing of open viscous fluidis, *Phys. Rev. Lett.*, **92** 038301 (2004).

63 Suzuki, H. and Ho, C. M., A magnetic force driven chaotic micro-mixer, *Proc. MEMS'02, 15th IEEE Int. Workshop Micro Electro Mechanical System (Las Vegas, Nevada)*, 40 (2002).

64 Lu, L. H., Ryu, K. S. and Liu, C., A magnetic microstirrer and array for microfluidic mixing, *J. Microelectromech. Syst.*, **11** 462 (2002).

65 El Moctar, A. O., Aubry, N. and Batton, J., Electro–hydrodynamic micro-fluidic mixer, *Lab Chip*, **3** 273 (2003).

66 Deval, J., Tabeling, P. and Ho, C. M., A dielectrophoretic chaotic mixer, *Proc. MEMS'02, 15th IEEE Int. Workshop Micro Electro Mechanical System (Las Vegas, Nevada)*, 36 (2002).

67 Lee, Y.-K., Deval, J., Tabeling, P. and Ho, C.-M. Chaotic mixing in electrokinetically and pressure driven micro flows, *Proc. MEMS'01, 14th IEEE Int. Workshop on Micro Electro Mechanical System (Interlaken, Switzerland)*, 483 (2001).

68 Jacobson, S. C., McKnight, T. E. and Ramsey, J. M., Microfluidic devices for electrokinematically driven parallel and serial mixing, *Anal. Chem.*, **71** 4455 (1999).

69 Lettieri, G. L., Dodge, A., Boer, G., Lichtenberg, J., Verpoorte, E. and de Rooij, N. F., Consequences of opposing electrokinetically and pressure-induced flows in microchannels of varying geometries, *Proc. MEMS'00, 13th IEEE Int. Workshop Micro Electro Mechanical System* (Enschede, NL), 351 (2000).

70 Oddy, M. H., Santiago, J. G. and Mikkelsen, J. C., Electrokinetic instability micromixing, *Anal. Chem.*, **73** 5822 (2001).

71 Tang, Z., Hong, S., Djukic, D., Modi, V., West, A. C., Yardley, J. and Osgood, R. M., Electrokinetic flow control for composition modulation in a microchannel, *J. Micromech. Microengg.*, **12** 870 (2002).

72 Bau, H. H., Zhong, J. and Yi, M., A minute magneto hydro dynamic (MHD) mixer, *Sensors Actuators B*, **79** 207 (2001).

73 Moroney, R. M., White, R. M. and Howe, R. T., Ultrasonically induced microtransport, *Proc. MEMS'91, 3rd IEEE Int. Workshop Micro Electro Mechanical System (Nara, Japan),* 277 (1991)

74 Zhu, X. and Kim, E. S., *Acoustic-wave liquid mixer*, Microelectromechanical Systems (MEMS), ASME, Dynamic Systems and Control Division (Publication), Fairfield, NJ, **62** 35 (1997).

75 Rife, J. C., Bell, M. I., Horwitz, J. S., Kabler, M. N., Auyeung, R. C. Y. and Kim, W. J., Miniature valveless ultrasonic pumps and mixers, *Sensors Actuators A*, **86** 135 (2000).

76 Vivek, V., Zeng, Y. and Kim, E. S., Novel acoustic-wave micromixer, *Proc. MEMS'00, 13th IEEE Int. Workshop Micro Electro Mechanical System (Miyazaci, Japan)*, 668 (2000).

77 Woias, P., Hauser, K. and Yacoub-George, E., An active silicon micromixer for μTAS applications, van den Berg, A., Olthuis, W., Bergveld, P., (Eds.)*, Micro Total Analysis Systems*, Kluwer Academic Publishers, Drodecht, 277 (2000).

78 Yasuda, K., Non-destructive, non-contact handling method for biomaterials in micro-chamber by ultrasound, *Sensors Actuators B*, **64** 128 (2000).

79 Yang, Z., Goto, H., Matsumoto, M. and Maeda, R., Active micromixer for microfluidic systems using lead-zirconate-titanate(PZT)-generated ultrasonic vibration, *Electrophoresis*, **21** 116 (2000).

80 Yang, Z., Matsumoto, S., Goto, H., Matsumoto, M. and Maeda, R., Ultrasonic micromixer for microfluidic systems, *Sensors Actuators A*, **93** 266 (2001).

81 Liu, R. H., Yang, J. N., Pindera, M. Z., Athavale, M. & Grodzinski, P., Bubble induced acoustic micromixing, *Lab Chip*, **2** 151 (2002).

82 Liu, R. H., Lenigk, R., Druyor-Sanchez, R. L., Yang, J. and Grodzinski, P., Hybridization enhancement using cavitation microstreaming, *Anal Chem.*, **75** 1911 (2003).

83 Yaralioglu G. G., Wygant I. O., Marentis T. C. and Khuri-Yakub B. T., Ultrasonic mixing in microfluidic channels using integrated transducers, *Anal. Chem.*, **76** 3694 (2004).

84 Mao, H., Yang, T. and Cremer, P. S., A microfluidic device with a linear temperature gradient for parallel and combinatorial measurements, *J. Am. Chem. Soc.*, **124** 4432 (2002).

85 Tsai, J. H. and Lin, L., Active microfluidic mixer and gas bubble filter driven by thermal bubble pump, *Sensors Actuators A*, **97–98** 665 (2002).

86 Chen, S. and Doolen, G. D., Lattice Boltzmann Method for Fluid Flows, *Ann. Rev. Fluid Mech.*, **30** 329 (1998).

87 Hazi, G., Imre, A. R., Mayer, G. and Farkas, I., Lattice Boltzmann methods for two-phase flow modeling, *Annals Nucl. Energy*, **29** 1421 (2002).

88 Yu, D., Mei, R., Luo, L.-S. and Shyy, W., Viscous flow computations with the method of lattice Boltzmann equation *Prog. Aero. Sci.*, **39** 329 (2003).

89 Nourgaliev, R. R., Dinh, T. N., Theofanous, T. G. and Joseph, D., The lattice Boltzmann equation method: Theoretical interpretation, numerics and implications, *Int. J. Multiphase Flow*, **29** 117 (2003).

90 Majumdar, A., *Microscale Energy Transport in Solids in Microscale Energy Transport*, Tien, C.-L., Majumdar, A. and Gerner, F.M. (Eds.), Taylor and Francis (1998).

91 McCracken, M. E. and Abraham, J., Multiple-relaxation-time lattice-Boltzmann model for multiphase flow, *Phys. Rev. E*, **71** 036701 (2005).

92 Asinari, P., Semi-implicit-linearized multiple-relaxation-time formulation of lattice Boltzmann schemes for mixture modeling, *Phys. Rev. E*, **73** 056705 (2006).

93 He, X. and Luo, L.-S., Theory of the lattice Boltzmann method: From the Boltzmann equation to the lattice Boltzmann equation *Phys. Rev. E*, **56** 6811 (1997).

94 Hou, S., Zou, Q., Chen, S., Doolen, G. and Cogley, A. C., Simulation of cavity flow by the lattice Boltzmann method, *J. Comp. Phys.*, **118** 329 (1995).

95 He, X. and Luo, L.-S., Lattice Boltzmann model for the incompressible Navier-Stokes equation, *J. Stat. Phys.*, **88** 927 (1997).

96 Zou, Q. and He, X., On pressure and velocity boundary conditions for the lattice Boltzmann BGK model, *Phys. Fluids*, **9** 1591 (1997).

97 Noble, D. R., Chen, S., Georgiadis, J. G. and Buckius, R. O., A consistent hydrodynamic boundary condition for the lattice Boltzmann method, *Phys. Fluids*, **7** 203 (1995).

98 Chen, S., Martinez, D. and Mei, R., On boundary conditions in lattice Boltzmann methods, *Phys. Fluids*, **8** 2527 (1996).

99 Guo, Z.-L., Zheng, C.-G. and Shi, B.-C., Non-equilibrium extrapolation method for velocity and pressure boundary conditions in the lattice Boltzmann method, *Chinese Phys.*, **11** 366 (2002).

100 Lim, C. Y., Shu, C., Niu, X. D. and Chew, Y. T., Application of lattice Boltzmann method to simulate microchannel flows, *Phys. Fluids*, **14** 2299 (2002).

101 Soong, C. Y. and Wang, S. H., Theoretical analysis of electrokinetic flow and heat transfer in a microchannel under asymmetric boundary conditions, *J. Colloid Interface Sci.*, **265** 203 (2003).

102 Towns, J. K. and Regnier, F. E., Capillary electrophoretic separations of proteins using nonionic surfactant coatings, *Anal. Chem.*, **63** 1126 (1991).

103 Masliyah, J. H. and Bhattacharya, S., *Electrokinetic and Colloidal Transport Phenomena*, John-Wiley & Sons, New Jersey (2006).

104 Qiao, R. and Aluru, N. R., Transient analysis of electro-osmotic transport by a reduced-order modelling approach, *Int. J. Numer. Methods Engg.*, **56** 1023 (2003).

105 Paul, P. H., Garguilo, M. G. and Rakestraw, D., Imaging of pressure- and electrokinetically driven flows through open capillaries, *Anal. Chem.*, **70** 2459 (1998).

106 Ng, A. S. W., Hau, W. L. W., Lee, Y. K. and Zohar, Y., Electrokinetic generation of microvortex patterns in a microchannel liquid flow, *J. Micromech. Microeng.*, **14** 247 (2004).

107 Qian, S. and Bau, H., A chaotic electroosmotic stirrer, *Anal. Chem.*, **74** 3616 (2002).

108 Stroock, A. D. and McGraw, G. J., Investigation of the staggered herringbone mixer with a simple analytical model, *Phil. Trans. R. Soc. Lond. A.*, **362** 971 (2004).

109 Pacheco, J. R., Chen, K. P. and Hayes, M. A., Rapid and efficient mixing in a slip-driven three-dimensional flow in a rectangular channel, *Fluid. Dyn. Res.*, **38** 503 (2006).

110 Kim, S. J., Kang, I. S. and Yoon, B. J., Electroosmotic helical flow produced by combined use of longitudinal and transversal electric fields in a rectangular microchannel, *Chem. Engg. Comm.*, **193** 1075 (2006).

111 Qian, S. and Bau, H. H., Theoretical investigation of electro-osmotic flows and chaotic stirring in rectangular cavities, *App. Math. Modeling*, **29** 726 (2005).

112 Ladd, A. J. C., Sedimentation of homogeneous suspensions of non-Brownian spheres, *Phys. Fluids*, **9** 491 (1997).

113 Succi, S., *The Lattice Boltzmann Equation for Fluid Dynamics and Beyond*, Oxford, New York, (2001)

114 Tang, G. H., Li, Z., Wang, J. K., He, Y. L. and Tao, Q., Electroosmotic flow and mixing in microchannels with the lattice Boltzmann method, *J. Appl. Phys.*, **100** 094908-1 (2006).

115 Melchionna, S. and Succi, S., Electrorheology in nanopores via lattice Boltzmann. Simulation, *J. Chem. Phys.*, **120** 4492 (2004).

116 Ng, A. S. W., Hau, W. L. W., Lee, Y. K. and Zohar, Y., Electrokinetic generation of microvortex patterns in a microchannel liquid flow, *J. Micromech. Microeng.*, **14** 247 (2004).

117 Chang, C. C. and Yang, R. J., Computational analysis of electrokinetically driven flow mixing in microchannels with patterned blocks, *J. Micromech. Microeng.*, **14** 550 (2004).

118 O'Neil, P. V., *Advanced Engineering Mathematics*, Pacific Grove, Thomson (2003).

119 de Vahl Davis, G., Natural Convection of air in a square cavity: A benchmark numerical solution, *Int. J. Num. Methods Fluids.*, **3** 249 (1983).

120 D'Orazio, A., Corcione, M. and Celata, G. P., Application to natural convection enclosed flows of a lattice Boltzmann BGK model coupled with a general purpose thermal boundary condition, *Int. J. Thermal Sci.*, **43** 575 (2004).

121 Mukhopadhyay, A., Ganguly, R., Sen, S. and Puri, I. K., A scaling analysis to characterize thermomagnetic convection, *Int. J. Heat Mass Transfer.*, **48** 3485 (2005).

122 Ghia, U., Ghia, K. N. and Shin, C. T., High-Re solutions for incompressible flow using the Navier Stokes equations and a multigrid method, *J. Comput. Phys.*, **48** 387 (1982).

123 Xia, H. M., Shu, C., Wan, S. Y. M. and Chew, Y. T., Influence of the Reynolds number on chaotic mixing in a spatially periodic micromixer and its characterization using dynamical system techniques, *J. Micromech. Microeng.*, **16** 53 (2006).

124 Camesasca1, M., Manas-Zloczower, I. and Kaufman, M., Entropic characterization of mixing in microchannels, *J. Micromech. Microeng.*, **15** 2038 (2005)

125 Chang, C. and Yang, R., *J. Micromech. Microeng.*, **16** 1453 (2006).

126 Elias, H., *Macromolecules 1 Structure and Properties*, Plenum, New York and London (1983).

127 Gijs, M. A. M., Magnetic bead handling on-chip: new opportunities for analytical applications, *Microfluid. Nanofluid.*, **1** 22 (2004).

128 Pamme, N., Magnetism and microfuidics, *Lab Chip*, **6** 24 (2006).

129 Suzuki, H., Ho, C.-M. and Kasagi, N., A Chaotic Mixer for Magnetic Beads-Based Micro Cell Sorter, *J. Microelectromech. Syst.*, **13** 779 (2004).

130 Melle, S., Fuller, G. G. and Rubio, M. A., Structure and dynamics of magnetorheological fluids in rotating magnetic fields, *Phys. Rev. E*, **61** 4111 (2000).

131 Kang, T. G., Hulsen, M. A., Anderson, P. D., den Toonder, J. M. J. and Meijer, H. E. H., Chaotic mixing induced by a magnetic chain in a rotating magnetic field, *Phys. Rev. E*, **76** 066303 (2007).

132 Ryu, K. S., Shaikh, K., Goluch, E., Fan, Z. F. and Liu, C. Micro magnetic stir-bar mixer integrated with parylene microfluidic channels, *Lab Chip***, 4** 608 (2004).

133 Oh, D. W., Jin, J. S., Choi, J. H., Kim, H. Y. and Lee, J. S., A microfluidic chaotic mixer using ferrofluid, *J. Micromech. Microeng.,* **17** 2077 (2007).

134 West, J., Karamata, B., Lillis, B., Gleeson, J. P., Alderman, J., Collins, J. K., Lane, W., Mathewson, A. and Berney, H., Application of magnetohydrodynamic actuation to continuous flow chemistry, *Lab Chip,* **2** 224 (2002).

135 Zborowski, M., Sun, L. P. and Moore, L. R., Continuous cell separation using novel magnetic quadrupole flow sorter. *J. Magn. Magn. Mater.*, **194** 224 (1999).

136 Hayes, M. A., Polson, N. A., Phayre, A. N. and Garcia, A. A., Flow-based microimmunoassay, *Anal. Chem.*, **73** 5896 (2001).

137 Rida, A. and Gijs, M. A. M., Dynamics of magnetically retained supraparticle structures in a liquid flow, *Appl. Phys. Lett.*, **85** 4986 (2004).

138 Wang, Y., Zhe, J., Chung, B. T. F. and Dutta, P., A rapid magnetic particle driven micromixer, *Microfluid. Nanofluid.*, **5** 375 (2005).

139 Rosensweig, R. E., *Ferrohydrodynamics*., Cambridge University Press, New York (1985).

140 Fertman, V. E., *Magnetic fluids guidebook: properties and applications*., Hemisphere, New York (1990).

141 Ganguly, R., Sen, S. and Puri, I. K., Thermomagnetic convection in a square enclosure using a line dipole, *Phys. Fluid.*, **16**, 2228 (2004).

142 Succi, S., Lattice Boltzmann equation: failure or success?, *Physica A.*, **240** 221 (1997).

143 Shan, X. W. and Doolen, G., Diffusion in a multicomponent lattice Boltzmann equation model, *Phys. Rev. E*, **54** 3614 (1996).

144 Swift, M. R., Orlandini, E., Osborn, W. R. and Yeomans, J. M., Lattice Boltzmann simulations of liquid-gas and binary fluid systems, *Phys. Rev. E*, **54** 5041 (1996).

145 Lamura, A., Gonnella, G. and Yeomans, J. M., A lattice Boltzmann model of ternary fluid mixtures, *Europhys. Lett.*, **45** 314 (1999).

146 Luo, L. S. and Girimaji, S. S., Theory of the lattice Boltzmann method: Two-fluid model for binary mixtures, *Phys. Rev. E*, **67,** 036302 (2003).

147 Bhatnagar, P. L., Gross, E. P. and Krook, M., A model for collisional processes in gases I: small amplitude processes in charged and neutral one-component system, *Phys. Rev.*, **94** 511 (1954).

148 Ganguly, R., Gaind, A. P., Sen, S. and Puri, I. K., Analyzing ferrofluid transport for magnetic drug targeting, *J. Magn. Magn. Mater.*, **289** 331 (2005).

149 Boss, J., Evaluation of homogeneity degree of a mixture, *Bulk solids handling*, **6** 1207 (1986).

150 Danckwerts, P., *The definition and measurement of some. characteristics of mixtures*, *Appl. Sci. Res. A*, **3** 279 (1952).

151 Stremler, M. A., Mixing measures, Li, D., (Ed.) *Encyclopedia of Microfluidics and Nanofluidics,* Springer. (2008).

152 Ganguly, R., Zellmer, B. and Puri, I. K., Field-induced self-assembled ferrofluid aggregation in pulsatile flow, *Phys. Fluid.*, **17** 097104 (2005).